Radboud University

Politecnico di Torino

Master degree in Nanotechnologies for ICTs

Surface Recombination Speed Determination and Simulations of GaAs-InGaP Solar Cells

Author:
Valerio Trinito

Supervisors:
Federica Cappelluti
Gerard Bauhuis

Contents

List of Symbols

q	elementary charge
ϵ_0	vacuum dielectric permittivity
ϵ_r	relative dielectric permittivity
h	planck's constant
$\hbar = \frac{h}{2\pi}$	reduced planck's constant
c	speed of light in vacuum
E	energy
$\mathcal{E}$	electric field
P_{opt}	optical power
P_{el}	electrical power
λ	wavelength
θ	incident angle
T	temperature
K_B	boltzmann constant
$V_T = \frac{K_B T}{q}$	thermal tension
$n(\lambda)$	complex refractive index
$n_A(\lambda)$	complex refractive index of the active region
α	absorption coefficient
E_G	energy band-gap
$q\chi$	workfunction
n_i	intrinsic carrier concentration
N_C^{eff}	conduction band density of states
N_V^{eff}	valence band density of states
d_E	n-doped active region thickness
d_B	p-doped active region thickness
d_1	emitter thickness
d_2	base thickness
L	active region thickness
N_D	n-doping of emitter active region
N_A	p-doping of base active region
n	free electrons' concentration
p	free holes' concentration
μ_n	electrons' mobility
μ_p	holes' mobility
D_n	electrons' diffusivity
D_p	holes' diffusivity
n_i	intrinsic carrier concentration

τ_n	electrons' lifetime
τ_p	holes' lifetime
L_n	electrons' diffusion length
L_p	holes' diffusion length
V	applied bias
S_n or S_b	electrons' bottom surface recombination speed
S_p or S_f	holes' top surface recombination speed
GaAs	Gallium Arsenide
AlInP	Alluminum Indium Phosphide
InGaP	Indium Gallium Phosphide
Au	Gold
Ag	Silver
MgF_2	Magnesium Fluoride
ZnS	Zinc Sulfide

1 | Introduction

The current climate crisis urges us more than ever to further explore other forms of energy sources different from fossil fuels.
One form of energy that is practically unlimited is the one provided by the sun under the form of electromagnetic radiation. This energy can be partially harvested through solar panels, which relies on thermal energy, and through solar cells, which converts the electromagnetic power into electrical power.
Solar cells are devices which exploits the energy provided by the photons to excite electrons to a higher energy levels and use them to produce an electrical current. There are many different types of solar cells both in terms of material used and in terms of structural complexity. The most basic solar cells consist of a simple n-p junction; this is the region where the conversion from optical to electrical power takes place. The n-doped region is called "Emitter" while the p-doped region is called "Base". The main mechanism can be seen in Fig.1.1.

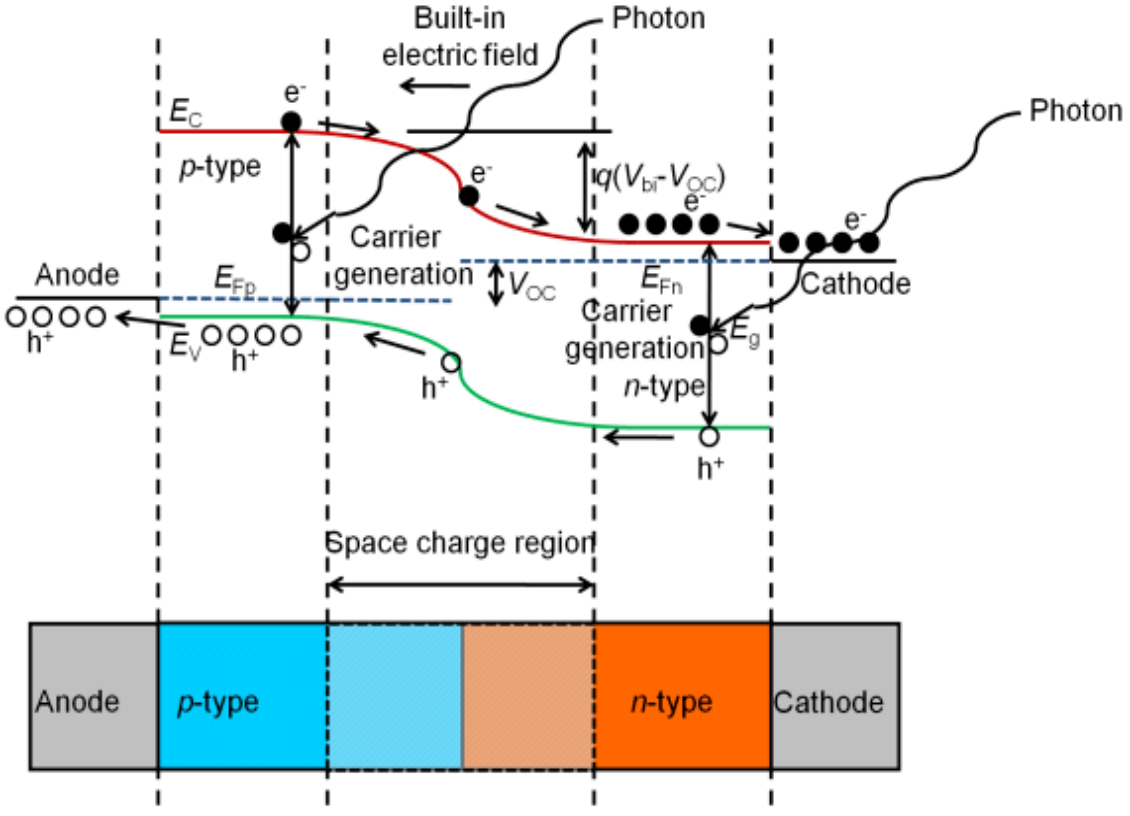

Figure 1.1: Schematic of the main mechanism of energy conversion in semiconductor n-p junctions solar cells. From [14]

Solar cells are characterized by three fundamental parameters: the short-circuit current (I_{sc}), the open-circuit voltage (V_{oc}) and the fill factor (FF). The product of these three parameters is the overall maximum power produced by the cell. Dividing the maximum power by the optical power impinging on the cell, the overall efficiency of the cell is determined. An example of the I-V characteristic of a solar cell under illumination can be observed in Fig.1.2.

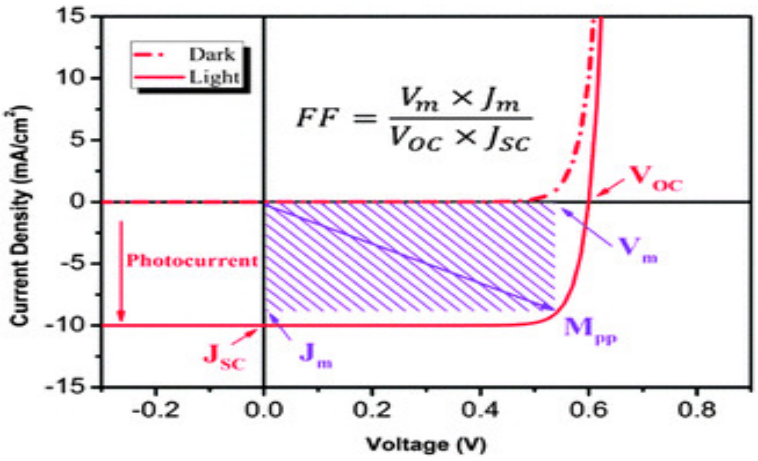

Figure 1.2: Example of the I-V characteristic of a solar cell under illumination. From [13]

Also important in defining the performances of solar cells are the internal quantum efficiency and the external quantum efficiency: the first is defined as the percentage of incident photons converted into generated electron-hole pairs for a certain wavelength; the external quantum efficiency is the product of the internal quantum efficiency and the collection efficiency, which is defined as the percentage of generated electron-hole pairs that gets actually collected by the metal contacts, becoming usable electrical current.
In order to improve the collection efficiency, a top layer called "window" and a bottom layer called "back surface field" are used. Usually, they are made of different materials with respect to the active region and their purpose is to prevent recombination of the generated holes and electrons at the metal contacts. In fact, to produce electrical current, the majority carriers need to be collected by the circuit without recombining with the minority carriers and a considerable part of the recombination happens at the metal contacts. The window and the back surface field act as reflectors of minority carriers so that only the majority carriers reach the contacts and they are not lost in recombination.
Many other techniques are used, starting from this base structure, to improve the cells efficiency: for example, multi-junction devices exploits different materials (with different bandgaps) in order to absorb photons at a wider range of wavelengths.
Nowadays, solar cells are often made of semiconductor materials, however, for instance, research and production of organic solar cells are on the rise. An overview of the type of cells and their efficiencies can be seen in Fig.1.3.

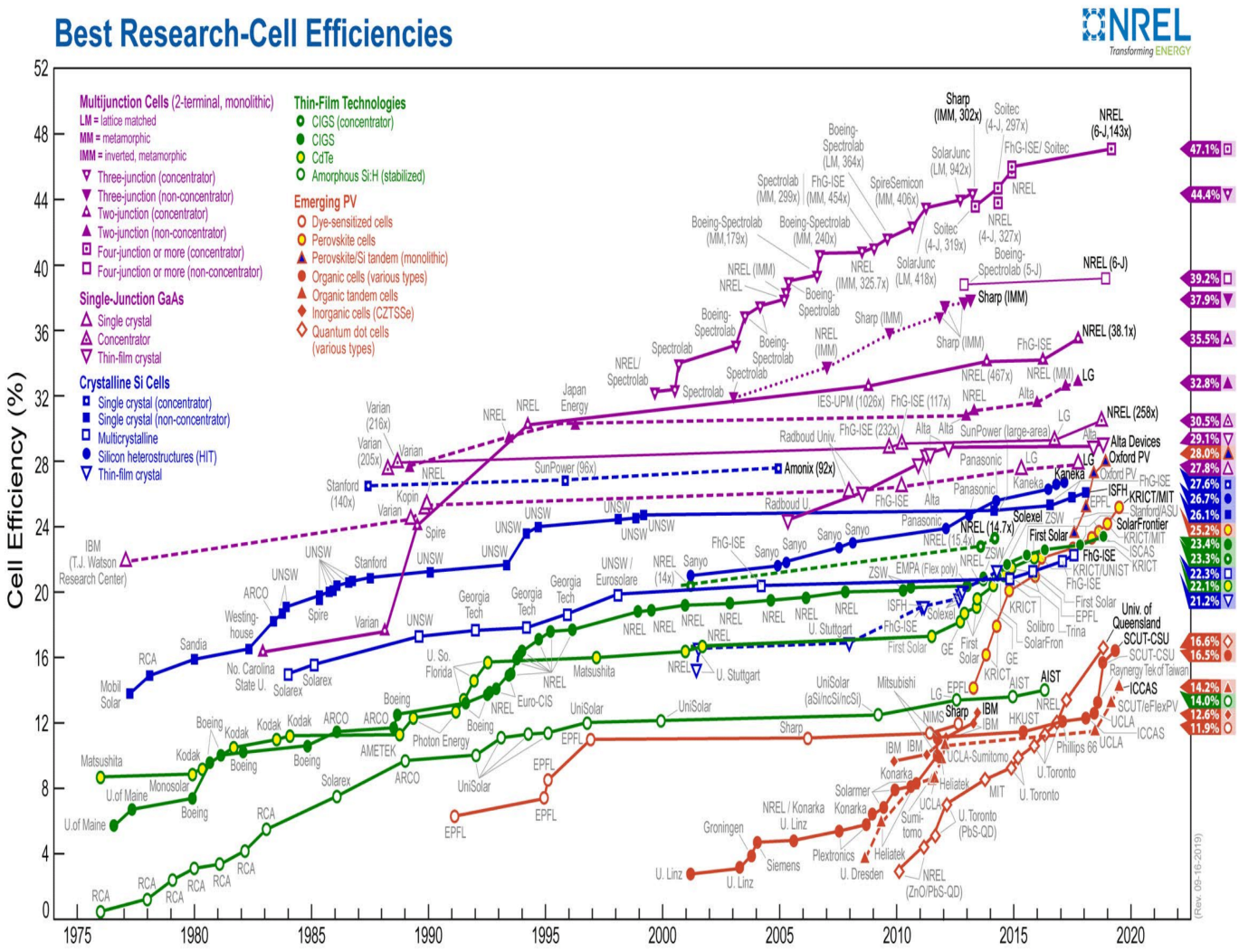

Figure 1.3: Best efficiencies achieved for different types of solar cells. From the "National Renewable Energy Laboratory" website: [15]

Solar cells for commercial applications are mainly silicon-based. In fact, Silicon, due to its abundance in nature, is characterized by relatively low cost with respect to other materials.
III-V materials, highlighted in Fig.1.4, are used to fabricate high efficiency solar cells. In fact, while Silicon is a good material for micro- and nano-electronics, most opto-electronic devices work better with direct bandgap semiconductors (such as Gallium Arsenide). Usually, these III-V based cells are employed for space applications where the importance of their efficiency and reliability overcomes their high cost.

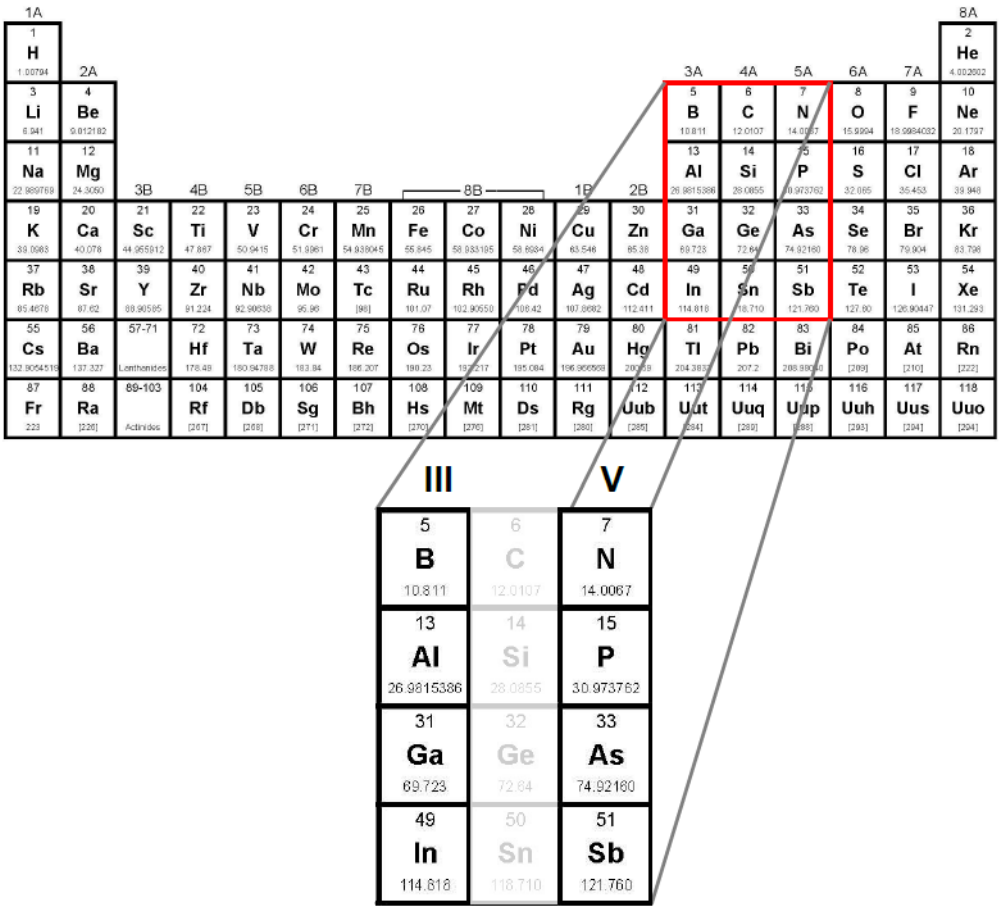

Figure 1.4: III-V materials used from the period table of elements. From [16]

In this work, GaAs based solar cells have been investigated. All the cells have been grown, processed and measured at the Applied Material Science at Radboud University. The processing and the measurements have been directly performed by the author of this thesis.

Analytical analysis of micro and nano-electronic devices is a very powerful tool to understand their behaviour.
The Hovel (or Shockley) model is largely employed for simulating solar cells. It is based on solving analytically the drift-diffusion and continuity equations of a p-n junction to predict the photovoltaic characteristics of a solar cell. This model relies on a number of strong approximations which make it not completely precise; however its efficacy has been proven in multiple works ([7]).
In this thesis, the Hovel model has been adapted to generic n-p heterojunction analysis; the model has been integrated with an analytical derivation of the photon recycling and with an exact method to treat the optics inside the cell.
The Hovel model relies on a series of optical and electrical input parameters describing the materials used. Some of these parameters are intrinsic, directly measurable material parameters which are already listed and easily accessible. Others are derived electrical parameters. Among the latter category, some can be derived analytically with very good approximation (for example, the radiative lifetime $\tau_{n/p}^{\mathrm{Rad}}$), while others are derived using empirical models. Empirical doping-and-temperature dependent models for the electron and hole Shockley-Read-Hall (SRH) recombination lifetimes and mobilities ($\tau_{n/p}^{\mathrm{SRH}}$ and $\mu_{n/p}$) have already been derived ([1] and [2]) and used in this work. However,

to our knowledge, no efficient model to determine the so-called "surface recombination speed" ("S") exists.
This electrical parameter describes the recombination velocity of minority carriers at an interface and it is fundamental to simulate the electrical behaviour of solar cells, diodes and transistors. In particular, for solar cells with very high efficiencies and with very good diffusion lengths with respect to the junction physical dimensions, the surface recombination speed has a high relevance in determining the overall performance.
In the Hovel model, the recombination rate of minority carriers at a given interface between two different materials (typically between emitter and window and between base and BSF) is computed as the product of the surface recombination speed and the excess minority carriers at the said interface. The surface recombination speed depends on a number of variables among which the superficial density of states and other physical characteristics of the interface. However, normally, the surface recombination speeds are considered to be independent from the excess minority carriers at the said interface, both in simulations and in measurements set-ups. In this work, this assumption is challenged.

Nowadays, there are two main methods, that we are aware of, to measure the surface recombination speed of an interface:

- the "two emitter fabrication quantum yield" ("TEFQY") technique ([11])
- the "time resolved photo-luminescence" ("TRPL") method ([9])

The first relies on measuring the quantum yield of two similar samples with different emitter thicknesses and fit the front surface recombination speed (S_f) and the emitter diffusion length using the Hovel model. The TRPL method consists in measuring the carriers lifetimes and, using multiple samples, the surface recombination speed value can be fitted.
Both these methods are affected by strong limitations and assumptions. In the TEFQY technique, the derived S_f values are subjected to high uncertainty. The TRPL technique relies on multiple samples, a very precise measurement set-up and assumes that the top and bottom surface recombination speeds are equal. Furthermore, both these methods assume that the emitter thickness does not affect the S_f and the diffusion length values: in this work, both these assumptions are challenged.

For these reasons, an innovative method to determine the top surface recombination speed of solar cells by means of processing GaAs-InGaP heterojunctions has been developed. These kind of cells are characterized by the fact that the dark current contribution of the InGaP base is negligible, meaning that the overall dark current with ideality factor equal to 1 is given approximately only by the emitter diffusion current. Using the analytical and empirical models to determine all the other parameters of the cell, it is possible to fit the top surface recombination speed of the GaAs-window interface.

In this work, the empirical relation between S_f and the emitter thickness (d_E) and doping (N_D) has been investigated. In fact, as mentioned earlier, we start exploring the possibility that the surface recombination speed depends on the excess minority carriers at the interface (p'_{int}), other than on the type and quality of the said interface; p'_{int} depends on the bias voltage applied, on d_E and N_D. A series of similar cells with different d_E and N_D values and identical interface quality have been grown, processed and measured, deriving for each the S_f value. Using the collected data, a first, approximated, empirical model has been derived and used to run an optimization program using the Hovel model. The resulting structure has been grown, processed and measured to validate the simulation results.

2 | Model

The simulations have been implemented using Matlab. A 1D model which integrates an optical and an electrical analysis has been employed.
The first analysis consists in an analytical description of the electromagnetic behaviour inside the p-n junction together with a routine which computes relevant reflectances and transmittances through the scattering matrix method.
The electrical simulation is based on an analytical solution of the drift-diffusion and continuity equations of a p-n junction not at equilibrium. The main assumption made to solve these two equations in closed form is to have a perfectly abrupt separation between the quasi-neutral regions (QNR) and the depletion region or space charge region (SCR). Furthermore, only the p-n junction with the active material(s) is considered, and the model takes into account the layers at the top and the bottom only under the form of the so-called surface recombination speeds and by considering their overall reflectances and transmittances. This approach obviously implies that the current contribution of the layers at both the top and bottom is assumed to be negligible.

The relevant active material parameters taken into account in our analysis are:

- Complex refractive index: $n(\lambda) = \beta'(\lambda) - j\alpha'(\lambda)$ (also needed for the layers at the top and at the bottom)
- Band gap: $E_G[J]$
- Workfunction: $q\chi[J]$
- Intrinsic carrrier concentrations: $n_i[\frac{1}{m^3}]$
- Conduction and valence band density of states: $N_C^{\text{eff}}, N_V^{\text{eff}}[\frac{1}{m^3}]$
- Electrical parameters (which will be discussed more in detail in sub-section 2.2.1)

2.1 Optical Analysis

2.1.1 Scattering Matrix Method

This method can be used to compute the reflectances and transmittances of any layer stack. The only input parameters are:

- wavelength (λ)
- incident angle (θ)
- layers' thicknesses (t_m)
- layers' complex refractive indexes ($n_m = \beta'_m(\lambda) - j\alpha'_m(\lambda)$)

The method assumes that the impinging electromagnetic wave comes from a source infinitely distant and that it will propagate infinitely (without being reflected) once transmitted through the layer stack. For these reasons, to avoid physically absurd results, both the incident and the final media's complex refractive indexes are set to be real.

Through the scattering matrix method (discussed more in depth in Appendix A), it is possible to derive the reflectances and transmittances of a whole layer stack:

$$r^{\mathrm{TE/TM}}(\lambda,\theta) = \frac{\mathcal{E}^{\mathrm{TE/TM}}_{\mathrm{reflected}}}{\mathcal{E}^{\mathrm{TE/TM}}_{\mathrm{incident}}} \tag{2.1}$$

$$t^{\mathrm{TE/TM}}(\lambda,\theta) = \frac{\mathcal{E}^{\mathrm{TE/TM}}_{\mathrm{transmitted}}}{\mathcal{E}^{\mathrm{TE/TM}}_{\mathrm{incident}}} \tag{2.2}$$

$$R^{\mathrm{TE/TM}}(\lambda,\theta) = \frac{P^{\mathrm{TE/TM}}_{\mathrm{opt,reflected}}}{P^{\mathrm{TE/TM}}_{\mathrm{opt,incident}}} \tag{2.3}$$

$$T^{\mathrm{TE/TM}}(\lambda,\theta) = \frac{P^{\mathrm{TE/TM}}_{\mathrm{opt,transmitted}}}{P^{\mathrm{TE/TM}}_{\mathrm{opt,incident}}} \tag{2.4}$$

In our situation, it is assumed that the impinging wave is on average half "TE" and half "TM" so that the overall reflectances and transmittances can be defined as:

$$R = \frac{1}{2}R^{\mathrm{TE}} + \frac{1}{2}R^{\mathrm{TM}} \tag{2.5}$$

$$T = \frac{1}{2}T^{\mathrm{TE}} + \frac{1}{2}T^{\mathrm{TM}} \tag{2.6}$$

Hence, thanks to this method, from an optical point of view it is possible to consider all the layers between the front and the active region of the cell and between the active region and the back of the cell just as single values of reflectances and transmittances (of course, for each value of the incident angle and wavelength). A schematic of the logical process can be seen in Fig.2.1.

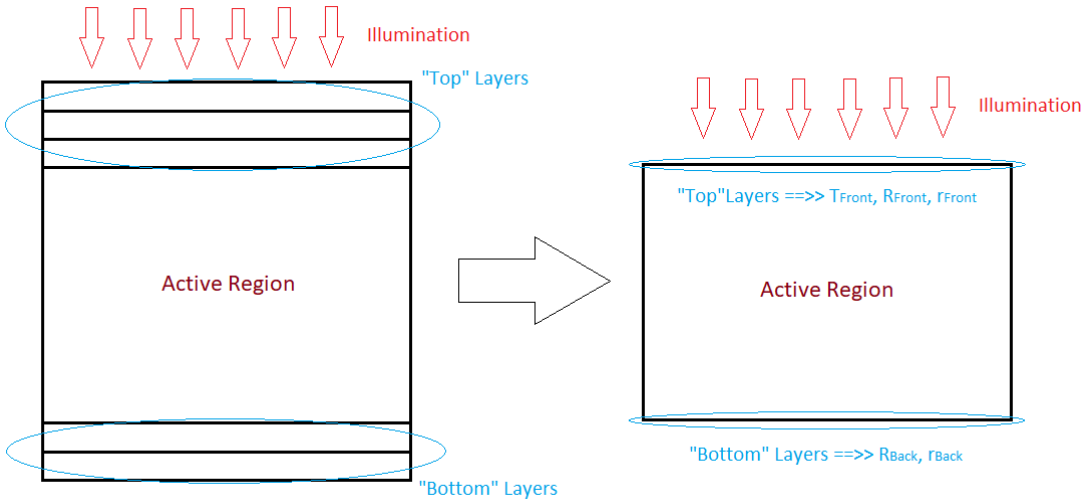

Figure 2.1: Schematic of the logical process of the optical analysis approach

2.1.2 Analytical Solution inside the n-p Junction

To compute the actual electromagnetic intensity inside the active region (n-p junction) of the cell, a zero incident angle is considered.
Let's define:

- Front layer stack reflectivity (considering the electromagnetic wave coming from the active region towards the front of the cell):

$$r_f(\lambda) = r^{TE}_{\text{Front,In==>Out}}(\lambda, \theta = 0) \tag{2.7}$$

- Front layer stack reflectance (considering the electromagnetic wave coming from the active region and going towards the front of the cell):

$$R_f(\lambda) = R_{\text{Front,In==>Out}}(\lambda, \theta = 0) \tag{2.8}$$

- Front layer stack transmittance (considering the electromagnetic wave coming from the front part of the cell and going towards the active region):

$$T_f(\lambda) = T_{\text{Front,Out==>In}}(\lambda, \theta = 0) \tag{2.9}$$

- Back layer stack reflectivity (considering the electromagnetic wave coming from the active region and going towards the back of the cell):

$$r_b(\lambda) = r^{\text{TE}}_{\text{Back,In==>Out}}(\lambda, \theta = 0) \tag{2.10}$$

- Back layer stack reflectance (considering the electromagnetic wave coming from the active region and going towards the back of the cell):

$$R_b(\lambda) = R_{\text{Back,In==>Out}}(\lambda, \theta = 0) \tag{2.11}$$

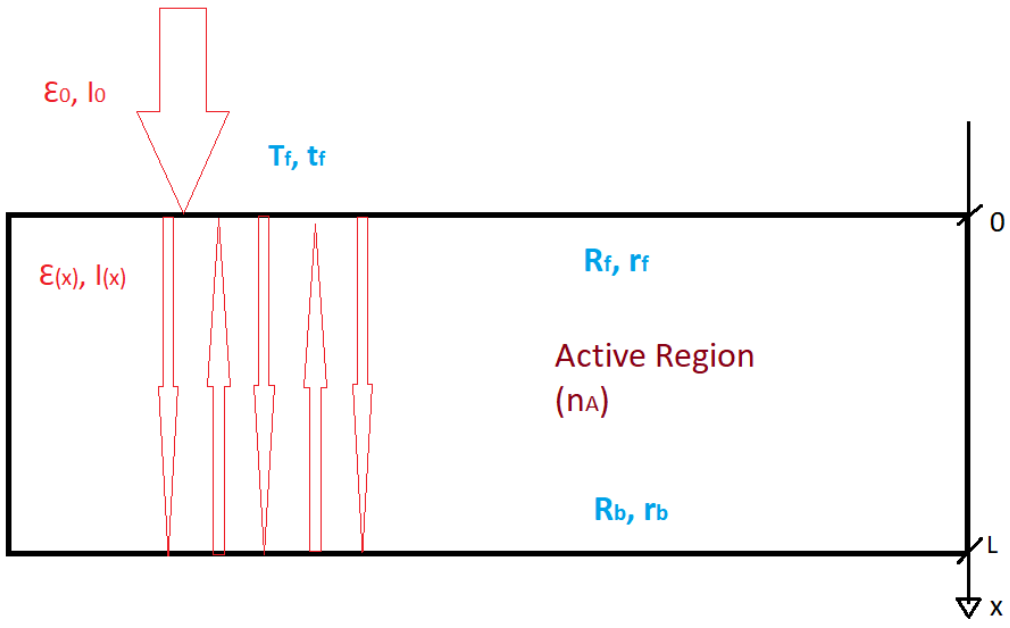

Figure 2.2: Schematic of the p-n junction optical analysis approach

Let's define:

- Wave number of the active region:

$$k_A = \frac{2\pi}{\lambda} n_A \tag{2.12}$$

- Absorption coefficient of the active region:

$$\alpha_A = \frac{4\pi}{\lambda} Im\left(-n_A\right) \tag{2.13}$$

- Double of the real part of the wave number of the active region:

$$\beta_A = \frac{4\pi}{\lambda} Re\left(n_A\right) \tag{2.14}$$

Referring to Fig.2.2 and considering the light to be coherent, it can be written:

$$\mathcal{E} = \mathcal{E}_0 t_f \left[e^{-jk_A x} + r_b e^{-jk_A L} e^{-jk_A (L-x)} + r_b r_f e^{-j2k_A L} e^{-jk_A x} + r_b^2 r_f e^{-j3k_A L} e^{-jk_A (L-x)} + r_b^2 r_f^2 e^{-j4k_A L} e^{-jk_A x} + ...\right] \tag{2.15}$$

Using the properties of infinite geometric series, Eq.2.15 can be developed in:

$$\mathcal{E} = \mathcal{E}_0 t_f \left[e^{-jk_A x} + r_b e^{-jk_A (2L-x)}\right] \times \left(\frac{1}{r_b r_f e^{-j2k_A L}}\right) \tag{2.16}$$

From this, the actual optical power inside the active region for each point on the x-axis is computed:

$$P_{\text{opt}} = \frac{n_A^2}{2Z_0} \mid \mathcal{E} \mid^2 = \left(\frac{1}{2Z_0} \mid \mathcal{E}_0 \mid^2\right) \left(n_A^2 \mid t_f \mid^2\right) \left|\left[e^{-jk_A x} + r_b e^{-jk_A (2L-x)}\right] \times \left(\frac{1}{r_b r_f e^{-j2k_A L}}\right)\right|^2 \tag{2.17}$$

$$P_{\text{opt}} = P_{\text{opt},0} T_f \left|\left[e^{-jk_A x} + r_b e^{-jk_A (2L-x)}\right] \times \left(\frac{1}{r_b r_f e^{-j2k_A L}}\right)\right|^2 \tag{2.18}$$

$$P_{\text{opt}} = P_{\text{opt},0} T_f e^{-j\alpha_A x} \left[\frac{1 + R_b e^{-2\alpha_A (L-x)} - 2e^{-\alpha_A (L-x)} Re\left(r_b e^{-j\beta_A (L-x)}\right)}{1 + R_b R_f e^{-2\alpha_A L} - 2e^{-\alpha_A L} Re\left(r_b r_f e^{-j\beta_A L}\right)}\right] \tag{2.19}$$

In terms of illumination, what matters are the number of incoming photons per wavelength and per unit area: "photon flux" (Φ_0).

$$\Phi_0 = \frac{P_{\text{opt},0}(\lambda)}{Area * E_{\text{photon}}(\lambda)} = \frac{P_{\text{opt},0}(\lambda)}{\left(Area * \frac{hc}{\lambda}\right)} \tag{2.20}$$

Hence, instead of the optical power inside the active region, the optical intensity is taken into account using eq.2.19 with Φ_0 instead of $P_{opt,0}$ as input:

$$\Phi = \Phi_0 T_f e^{-j\alpha_A x} \left[\frac{1 + R_b e^{-2\alpha_A (L-x)} - 2e^{-\alpha_A (L-x)} Re\left(r_b e^{-j\beta_A (L-x)}\right)}{1 + R_b R_f e^{-2\alpha_A L} - 2e^{-\alpha_A L} Re\left(r_b r_f e^{-j\beta_A L}\right)}\right] \tag{2.21}$$

2.2 Electrical Analysis

As mentioned in the introduction, the electrical analysis is based on solving both the drift-diffusion and continuity equations in closed form in the n-p junction domain. To do so, it is necessary to assume an abrupt separation between the n-doped quasi neutral region and the space charge region and between the space charge region and the p-doped quasi neutral region. This can be seen from Fig.2.3.

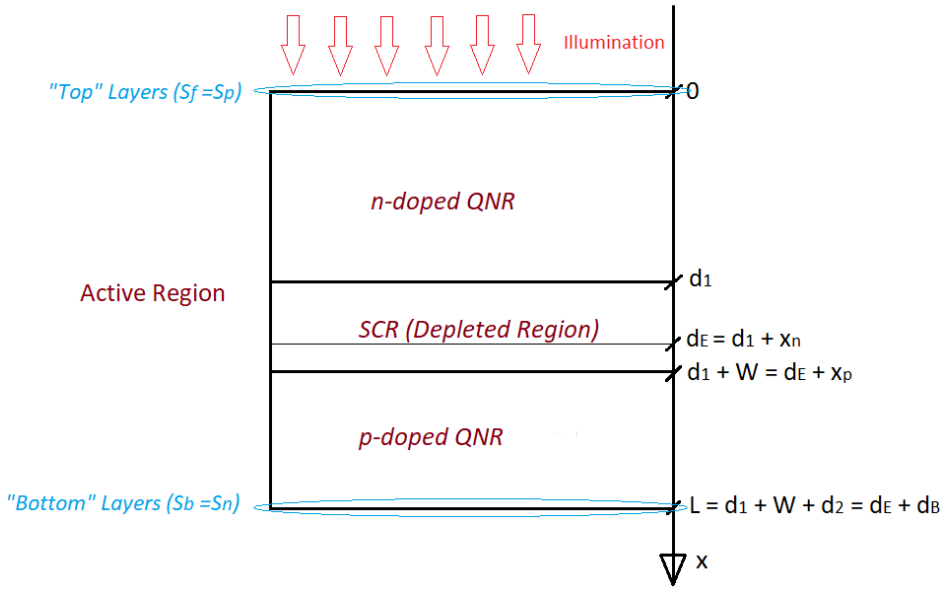

Figure 2.3: Schematic of the n-p junction model

It can be seen that d_E and d_B are the emitter and base thicknesses respectively, whereas x_n and x_p are the thicknesses of the depleted n-doped and p-doped part respectively; $W = x_n + x_p$ is the total SCR thickness and finally $d_1 = d_E - x_n$ and $d_2 = d_B - x_p$ are the thicknesses of the n-doped and p-doped QNRs respectively.

While d_E and d_B are given by the cell's growth process, the other quantities are derived assuming an abrupt separation between the QNRs and the SCR:

$$W = \sqrt{\left(\frac{2\epsilon_0\epsilon_r}{q}\right)\left(\frac{N_A + N_D}{N_A N_D}\right)(V_{built-in} - V)} \tag{2.22}$$

$$x_n = \frac{N_A}{N_A + N_D} W \tag{2.23}$$

$$x_p = \frac{N_A}{N_A + N_D} W \tag{2.24}$$

where V is the voltage applied, N_A and N_D are the dopant concentrations and:

$$V_{\text{built-in}} = V_T ln\left(\frac{N_A N_D}{n_i^2}\right) \tag{2.25}$$

$V_{built-in}$ has been derived assuming the Boltzmann statistics and complete ionization (of the dopant atoms).

The Hovel model implies the superposition assumption according to which the cell's total current density is given by the current in the dark (without illumination), which is given by a diode characteristic, summed with the photo-current (current generated only due to the illumination):

$$J^{\text{Tot}} = J^{\text{Photo}} + J^{\text{Dark}} \tag{2.26}$$

It is worth mentioning that, for the photo-current, it is assumed that the collection efficiency of the electrons and holes generated in the depleted region is equal to 1.

In general, the dark current density of a junction is given by:

$$J^{\text{Dark}} = J_{01}\left(e^{\frac{V}{V_T}} - 1\right) + J_{02}\left(e^{\frac{V}{2V_T}} - 1\right) + \left(\frac{Perimeter}{Area}\right) J_{\text{Perimeter}} \tag{2.27}$$

The first term is related to the minority carriers diffusion currents in the quasi neutral regions, the second one is due to the non-radiative recombination in the depleted region while, the third, to the perimeter non-radiative recombination due to the dangling bonds at the surface of the active material of the junction. Each term is associated to a, so-called, "ideality factor" (η). The first term is characterized by $\eta = 1$, the second by $\eta = 2$, while $J_{\text{Perimeter}}$ changes its slope with the voltage (starting from $\eta = 2$ for lower voltages and arriving at $\eta = 1$ at higher voltages ([6])). An example can be seen in Fig.2.4.

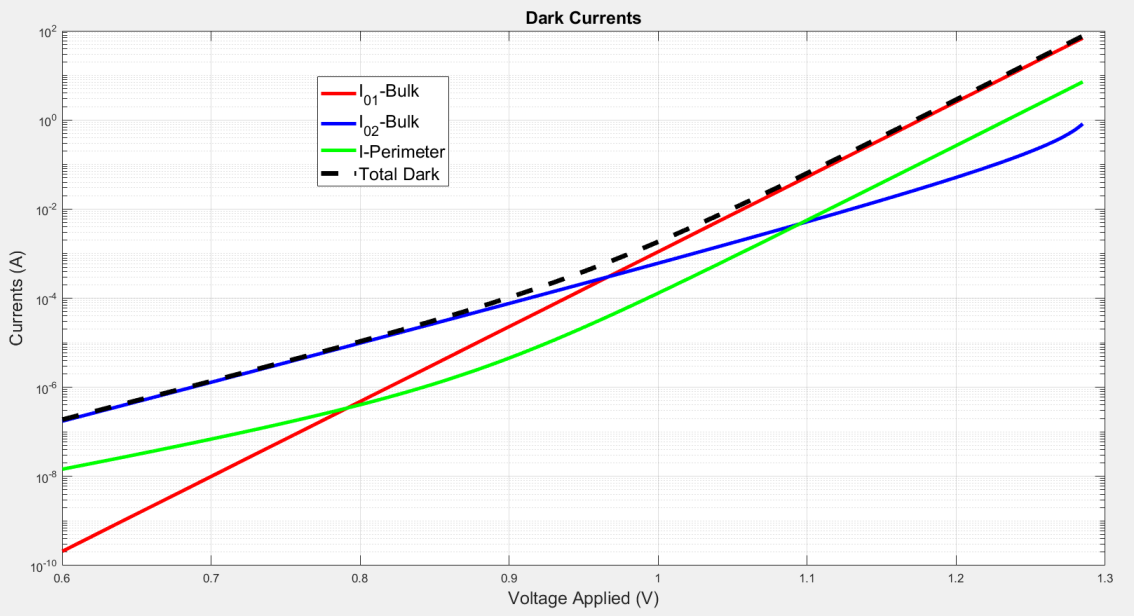

Figure 2.4: Example of a junction I-V characteristic's components for a GaAs homojunction cell

2.2.1 Electrical Parameters

The electrical parameters employed in the simulations are:

- Electron and hole mobilities: μ_n and μ_p derived through an empirical doping and temperature dependent model in [1].
- Electron and hole diffusivities: D_n and D_p defined through the "Einstein relation": $D_{n/p} = V_T \mu_{n/p}$.
- Electron and hole SRH lifetimes: τ_n^{SRH} and τ_p^{SRH} derived through an empirical doping and temperature dependent model in [2].
- Electron and hole radiative lifetimes: τ_n^{Rad} and τ_p^{Rad} computed thanks to: $\tau_n^{\text{Rad}} = \frac{1-f_{pr}}{BN_A}$ and $\tau_p^{\text{Rad}} = \frac{1-f_{pr}}{BN_D}$. A more detailed explanation of these parameters is given in 2.2.2 and 2.2.3.
- Electron and hole total lifetimes: τ_n and τ_p computed as: $\frac{1}{\tau_{n/p}} = \frac{1}{\tau_{n/p}^{\text{Rad}}} + \frac{1}{\tau_{n/p}^{\text{SRH}}}$. (Auger recombination has been neglected.)
- Electron and hole diffusion lengths: L_n and L_p computed as: $L_{n/p} = \sqrt{D_{n/p}\tau_{n/p}}$.

2.2.2 Radiative Lifetimes

Let's define the spontaneous emission rate (hence spontaneous recombination rate) of a semiconductor material at thermal equilibrium:

$$U_{\text{emission0}} = Bn_i^2 \tag{2.28}$$

and Not at thermal equilibrium (assuming $(E - qV) >> K_BT$:

$$U_{\text{emission}} = Bnp \tag{2.29}$$

An analytical formula has been derived in [3]:

$$B = \frac{2}{\pi^2\hbar^4c^3n_i^2}\int_0^{+\infty}\frac{\beta'^2E^3\alpha'}{e^{\frac{E}{K_BT}}-1}dE \tag{2.30}$$

At thermal equilibrium, the spontaneous recombination and generation rates are equal: $U_{\text{emission0}} = G_0$. Given that the radiative recombination rate of a semiconductor material can be written as:

$$U_{\text{Rad}} = U_{\text{emission}} - G_0 = U_{\text{emission}} - U_{\text{emission0}} \tag{2.31}$$

and, assuming that in a n-doped semiconductor $n \approx N_D$ and in a p-doped one $p \approx N_A$, it can be easily obtained:

$$U_{\text{Rad,n}} = BN_A\left(n - n_0\right) \tag{2.32}$$

$$U_{\text{Rad,p}} = BN_D\left(p - p_0\right) \tag{2.33}$$

where n_0 and p_0 are the minority carriers concentrations at thermal equilibrium for a p-doped and a n-doped semiconductor material respectively.

Defining now the excess minority carriers as $n' = n - n_0$ and $p' = p - p_0$, and the radiative recombination rates as:

$$U_{\text{Rad,n}} = \frac{n'}{\tau^{\text{Rad}_n}} \tag{2.34}$$

$$U_{\text{Rad,p}} = \frac{p'}{\tau_p^{\text{Rad}}} \tag{2.35}$$

Combining Eq.2.32 and Eq.2.34 and combining Eq.2.33 and Eq.2.35, it is straightforward to obtain:

$$\tau_n^{\text{Rad}} = \frac{1}{BN_A} \tag{2.36}$$

$$\tau_p^{\text{Rad}} = \frac{1}{BN_D} \tag{2.37}$$

2.2.3 Photon-Recycling Factor

The photon-recycling (pr) concept consists in taking into account that part of the emitted photons in the semiconductor will be re-absorbed by the semiconductor itself. This phenomenon can be modelled considering that in Eq.2.31 another generation term has to be added:

$$U_{\text{Rad}} = U_{\text{emission}} - G_0 - G_{pr} = U_{\text{emission}} - U_{\text{emission0}} - f_{pr}\left(U_{\text{emission}} - U_{\text{emission0}}\right) \tag{2.38}$$

obtaining:

$$U_{\text{Rad}} = (1 - f_{pr})\, B \left(np - n_i^2\right) \tag{2.39}$$

where f_{pr} is the so-called photon recycling factor.

Taking this added term into account in the treatise in 2.2.2, it is derived:

$$\tau_n^{\text{Rad}} = \frac{(1 - f_{pr})}{BN_A} \tag{2.40}$$

$$\tau_p^{\text{Rad}} = \frac{(1 - f_{pr})}{BN_D} \tag{2.41}$$

The f_{pr} value has been computed according to the theory displayed in [4]. Fig.2.5 shows a schematic of the cell according to the model. The main assumption is the uniform and isotropic emission of photons which implies that interference effects can be neglected and the treatise is in terms of intensity. Furthermore, the top and bottom layers are taken into account only under the form of the overall reflectance and transmittance and the probability of a photon to escape from the back is considered to be zero (with very good approximation). Finally the lateral dimensions of the cell are considered to be infinite with respect to the thickness (x axis).

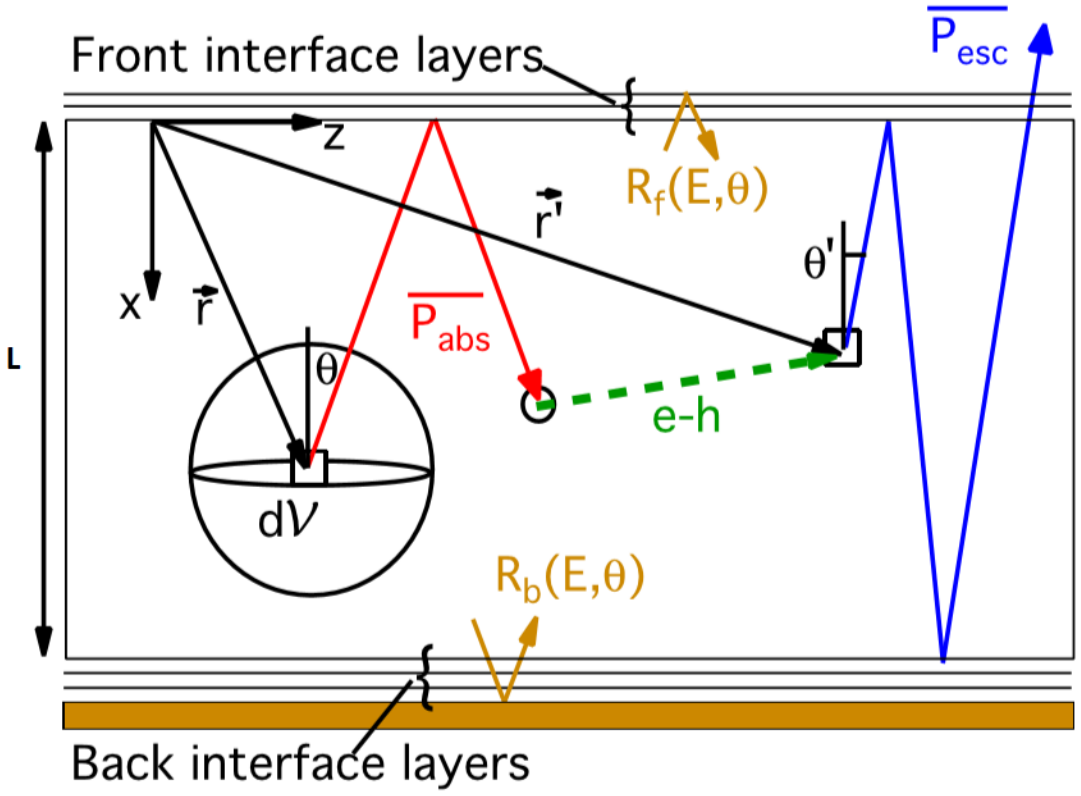

Figure 2.5: Geometry for modeling photon recycling (from [4])

The probabilities of a photon generated inside the cell to escape and to be absorbed, given a certain wavelength (hence energy), point and direction of emission, are given by:

$$P_{\text{esc}}(\lambda, x, \theta, \phi) = T_f \frac{e^{-\frac{\alpha x}{cos(\theta)}} + R_b e^{-\frac{\alpha(2L-x)}{cos(\theta)}}}{1 - R_f R_b e^{-\frac{2\alpha L}{cos(\theta)}}} \tag{2.42}$$

$$P_{\text{abs}}(\lambda, x, \theta, \phi) = 2 - \frac{\left(e^{-\frac{\alpha x}{cos(\theta)}} + e^{-\frac{\alpha(L-x)}{cos(\theta)}}\right)\left(1 - R_f R_b e^{-\frac{\alpha L}{cos(\theta)}}\right) - \left(1 - e^{-\frac{\alpha L}{cos(\theta)}}\right)\left(R_f e^{-\frac{\alpha x}{cos(\theta)}} + R_b e^{-\frac{\alpha(L-x)}{cos(\theta)}}\right)}{1 - R_f R_b e^{-\frac{2\alpha L}{cos(\theta)}}} \tag{2.43}$$

The average probability of generated photons to be re-absorbed correspond to the "photon-recycling factor" and it is given by:

$$f_{pr} = \overline{P_{\text{abs}}} = \frac{1}{4\pi Volume} \int_0^{+\infty} \widehat{S}(E) \int_0^{Volume} \int_0^{+\pi/2} \int_0^{+2\pi} P_{\text{abs}}(\lambda, x, \theta, \phi) sin(\theta) d\phi d\theta dV dE \tag{2.44}$$

Simplifying the area and the 2π, it is obtained:

$$f_{pr} = \overline{P_{\text{abs}}} = \frac{1}{2L} \int_0^{+\infty} \widehat{S}(E) \int_0^{L} \int_0^{+\pi/2} P_{\text{abs}}(\lambda, x, \theta) sin(\theta) d\theta dx dE \tag{2.45}$$

Where $\widehat{S}(E)$ is the normalized "spontaneous emission rate density":

$$\widehat{S}(E) = \frac{\frac{2}{\pi^2 \hbar^4 c^3} \frac{\beta'^2 E^3 \alpha'}{e^{\frac{E-qV}{K_B T}} - 1}}{\frac{2}{\pi^2 \hbar^4 c^3} \int_0^{+\infty} \frac{\beta'^2 E^3 \alpha'}{e^{\frac{E-qV}{K_B T}} - 1} dE} \tag{2.46}$$

Assuming $(E - qV) >> K_B T$,

$$\widehat{S}(E) = \frac{\beta'^2 E^3 \alpha' e^{\frac{-E}{K_B T}}}{\int_0^{+\infty} \beta'^2 E^3 \alpha' e^{\frac{-E}{K_B T}} dE} \tag{2.47}$$

2.2.4 J_{01}^{Dark} AND J^{Photo}

As mentioned in the chapter introduction, considering only the minority carriers diffusion currents originated in the emitter and in the base, it is possible to solve in a closed-form the second order differential equations in the quasi-neutral regions. Solving these equations the currents with an ideality factor of 1 and the emitter and base photo-currents are derived. More in depth explanation is provided in Appendix B. Furthermore, to these currents, it is added the photo-current originated in the depleted region assuming that the electrons and holes optically generated have an ideal collection efficiency (equal to 1). In general, the overall dark current with ideality factor of 1 and the overall photo-current are given by:

$$J^{\text{Photo}} = J_p^{\text{Photo}} + J_n^{\text{Photo}} + J_W^{Photo} \tag{2.48}$$

$$J_{01}^{\text{Dark}} = J_p^{\text{Dark}} + J_n^{\text{Dark}} \tag{2.49}$$

where:

$$J_p^{\text{Dark}} = J_{01,p} \left(e^{\frac{V}{V_T}} - 1\right) \tag{2.50}$$

$$J_n^{\text{Dark}} = J_{01,n} \left(e^{\frac{V}{V_T}} - 1\right) \tag{2.51}$$

$$J_{01}^{\text{Dark}} = (J_{01,n} + J_{01,p})\left(e^{\frac{V}{V_T}} - 1\right) = J_{01}\left(e^{\frac{V}{V_T}} - 1\right) \tag{2.52}$$

It is obtained:

- n-doped QNR:

$$J_p^{\text{Tot}} = J_p^{\text{Photo}} + J_p^{\text{Dark}} \tag{2.53}$$

where:

$$J_p^{\text{Dark}} = -\left(\frac{qD_p n_i^2}{L_p N_D}\frac{\sinh\left(\frac{d_1}{L_p}\right) + \frac{S_p L_p}{D_p}\cosh\left(\frac{d_1}{L_p}\right)}{\cosh\left(\frac{d_1}{L_p}\right) + \frac{S_p L_p}{D_p}\sinh\left(\frac{d_1}{L_p}\right)}\right)\left(e^{\frac{V}{V_T}} - 1\right) \tag{2.54}$$

$$J_p^{\text{Photo}} = \int_0^{+\infty} F_p\left[\frac{\frac{\partial z_p}{\partial x}|_{x=0} - \frac{S_p}{D_p}z_p(\lambda,0)}{\cosh\left(\frac{d_1}{L_p}\right) + \frac{S_p L_p}{D_p}\sinh\left(\frac{d_1}{L_p}\right)} + \frac{r_p}{L_p}z_p(\lambda,d_1) - \frac{\partial z_p}{\partial x}|_{x=d_1}\right]d\lambda \tag{2.55}$$

with:

$$F_p = \frac{q\Phi_0 T_f L_p^2 \alpha_A}{1 + R_b R_f e^{-2\alpha_A L} - 2e^{-\alpha_A L} Re\left(r_b r_f e^{-j\beta_A L}\right)} \tag{2.56}$$

$$z_p = \frac{e^{-\alpha_A x}}{1-(\alpha L_p)^2} + \frac{R_b e^{-2\alpha_A L} e^{\alpha_A x}}{1-(\alpha_A L_p)^2} + \frac{2e^{-\alpha_A L}}{1+(\beta_A L_p)^2} Re\left(r_b e^{-j\beta_A L} e^{j\beta_A x}\right) \tag{2.57}$$

$$r_p = \frac{\sinh\left(\frac{d_1}{L_p}\right) + \frac{S_p L_p}{D_p}\cosh\left(\frac{d_1}{L_p}\right)}{\cosh\left(\frac{d_1}{L_p}\right) + \frac{S_p L_p}{D_p}\sinh\left(\frac{d_1}{L_p}\right)} \tag{2.58}$$

- p-doped QNR:

$$J_n^{\text{Tot}} = J_n^{\text{Photo}} + J_n^{\text{Dark}} \tag{2.59}$$

where:

$$J_n^{\text{Dark}} = -\left(\frac{qD_n n_i^2}{L_n N_D}\frac{\sinh\left(\frac{d_2}{L_n}\right) + \frac{S_n L_n}{D_n}\cosh\left(\frac{d_2}{L_n}\right)}{\cosh\left(\frac{d_2}{L_n}\right) + \frac{S_n L_n}{D_n}\sinh\left(\frac{d_2}{L_n}\right)}\right)\left(e^{\frac{V}{V_T}} - 1\right) \tag{2.60}$$

$$J_n^{\text{Photo}} = \int_0^{+\infty} F_n\left[-\frac{\frac{\partial z_n}{\partial x}|_{x=L} + \frac{S_n}{D_n}z_n(\lambda,L)}{\cosh\left(\frac{d_2}{L_n}\right) + \frac{S_n L_n}{D_n}\sinh\left(\frac{d_2}{L_n}\right)} + \frac{r_n}{L_n}z_n(\lambda,x_p) + \frac{\partial z_n}{\partial x}|_{x=x_p}\right]d\lambda \tag{2.61}$$

with:

$$F_n = \frac{q\Phi_0 T_f L_n^2 \alpha_A}{1 + R_b R_f e^{-2\alpha_A L} - 2e^{-\alpha_A L} Re\left(r_b r_f e^{-j\beta_A L}\right)} \tag{2.62}$$

$$z_n = \frac{e^{-\alpha_A(x+d_E)}}{1-(\alpha_A L_n)^2} + \frac{R_b e^{-2\alpha_A L} e^{\alpha_A(x+d_E)}}{1-(\alpha_A L_n)^2} + \frac{2e^{-\alpha_A L}}{1+(\beta_A L_n)^2} Re\left(r_b e^{-j\beta_A L} e^{j\beta_A(x+d_E)}\right) \tag{2.63}$$

$$r_n = \frac{\sinh\left(\frac{d_2}{L_n}\right) + \frac{S_n L_n}{D_n}\cosh\left(\frac{d_2}{L_n}\right)}{\cosh\left(\frac{d_2}{L_n}\right) + \frac{S_n L_n}{D_n}\sinh\left(\frac{d_2}{L_n}\right)} \tag{2.64}$$

- SCR (Depleted Region):

$$J_W^{\text{Tot}} = J_W^{\text{Photo}} \tag{2.65}$$

where:

$$J_W^{\text{Photo}} = \int_0^{+\infty} F_W\left(z_{W,1} + z_{W,2} + z_{W,3}\right)d\lambda \tag{2.66}$$

with:

$$F_W = \frac{q\Phi_0 T_f}{1 + R_b R_f e^{-2\alpha_A L} - 2e^{-\alpha_A L} Re\left(r_b r_f e^{-j\beta_A L}\right)} \tag{2.67}$$

$$z_{W,1} = e^{-\alpha_A d_1}\left(1 - e^{-\alpha_A W}\right) \tag{2.68}$$

$$z_{W,2} = R_b e^{-\alpha_A (2L - d_1)}\left(e^{\alpha_A W} - 1\right) \tag{2.69}$$

$$z_{W,3} = 2\frac{\alpha_A}{\beta_A} e^{-\alpha_A L} Im\left(r_b e^{-j\beta_A (L - d_1)}\left(e^{j\beta_A W} - 1\right)\right) \tag{2.70}$$

2.3 HeteroJunction

Up to this point, the problem has been analyzed considering that the junction is made by one material only. In this work, model has been extended to simulate a n-p heterojunction. The theory behind the analysis of a junction with the n-doped side made by one material and the p-doped one by another is very similar to the theory behind a classic homojunction with few further considerations.

2.3.1 Optical Analysis

Two sets of front and back reflectances and transmittances have been computed:

- "-Top" is the apex that specifies that we are considering the front and back reflectances and transmittances considering only the n-doped material as the active region. In this case, the p-doped active material becomes one of the "back" layers.
- "-Bot" is the apex that specifies that we are considering the front and back reflectances and transmittances considering only the p-doped material as the active region. In this case, the n-doped active material becomes one of the "top" layers.

The previous analysis is modified to add the consideration that, optically, we have two different regions in the n-p junction:

$$\Phi^{\text{Top}}(\lambda, x) = \Phi_0 T_f^{\text{Top}} e^{-j\alpha_1 x}\left[\frac{1 + R_b^{\text{Top}} e^{-2\alpha_1 (d_E - x)} - 2e^{-\alpha_1 (d_E - x)} Re\left(r_b^{\text{Top}} e^{-j\beta_A (d_E - x)}\right)}{1 + R_b^{\text{Top}} R_f^{\text{Top}} e^{-2\alpha_1 d_E} - 2e^{-\alpha_1 d_E} Re\left(r_b^{\text{Top}} r_f^{\text{Top}} e^{-j\beta_1 d_E}\right)}\right] \tag{2.71}$$

$$\Phi^{\text{Bot}}(\lambda, x) = \Phi_0 T_f^{\text{Bot}} e^{-j\alpha_2 x}\left[\frac{1 + R_b^{\text{Bot}} e^{-2\alpha_2 (d_B - x)} - 2e^{-\alpha_2 (d_B - x)} Re\left(r_b^{\text{Bot}} e^{-j\beta_2 (d_B - x)}\right)}{1 + R_b^{\text{Bot}} R_f^{\text{Bot}} e^{-2\alpha_2 d_B} - 2e^{-\alpha_2 d_B} Re\left(r_b^{\text{Bot}} r_f^{\text{Bot}} e^{-j\beta_2 d_B}\right)}\right] \tag{2.72}$$

2.3.2 Built-in Potential and Depleted Region

The built-in potential is computed as:

$$-qV_{\text{built-in}} = q\Phi_1 - q\Phi_2 \tag{2.73}$$

where we can write:

$$q\Phi_1 = q\chi_1 + (E_{C,1} - E_{F,1}) \tag{2.74}$$

$$q\Phi_2 = q\chi_2 + (E_{C,2} - (E_{F,2} - E_{V,2})) \tag{2.75}$$

Since Boltzmann Statistics is considered:

$$n = N_C e^{-\frac{E_C - E_F}{K_B T}}, p = N_V e^{-\frac{E_F - E_V}{K_B T}} \tag{2.76}$$

it can be easily derived:

$$-qV_{\text{built-in}} = -\Delta Ec - E_{G2} + K_B T ln\left(\frac{N_C N_V}{N_D N_A}\right) \tag{2.77}$$

Of course, if the material 1 is the same as the material 2, $\Delta E_C = 0$ and, considering that $E_G = K_B T ln\left(\frac{N_C N_V}{n_i^2}\right)$, we obtain Eq.2.25 again.

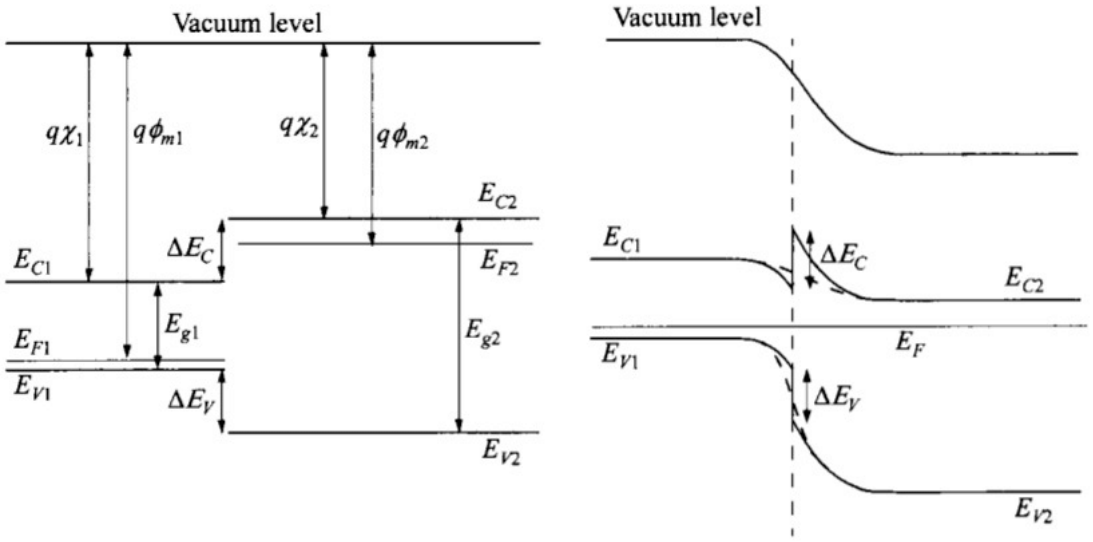

Figure 2.6: Band Diagram of a generic p-n Abrupt HeteroJunction

The depleted region thickness equation, taking into account the electric field discontinuity due to the relative permittivity discontinuity in the n-p junction domain, becomes:

$$W = \sqrt{\left(\frac{2\epsilon_0}{q}\right)\left(\frac{(N_A + N_D)^2}{(N_A N_D)\left(\frac{N_A}{\epsilon_{r,1}} + \frac{N_D}{\epsilon_{r,2}}\right)}\right)(V_{\text{built-in}} - V)} \tag{2.78}$$

2.3.3 J^{Dark} AND J^{Photo}

The homojunction treatise still holds but we take into account the different parameters for the n-doped and the p-doped materials and the different reflectances and transmittances. The subscripts "-1" and "-2" are used for the n-doped material and the p-doped material respectively.

It is obtained:

- n-QNR:

$$J_p^{\text{Tot}} = J_p^{\text{Photo}} + J_p^{\text{Dark}} \tag{2.79}$$

where:

$$J_p^{\text{Dark}} = -\left(\frac{qD_{p,1}n_{i,1}^2}{L_{p,1}N_D}\frac{sinh\left(\frac{d_1}{L_{p,1}}\right) + \frac{S_p L_{p,1}}{D_{p,1}}cosh\left(\frac{d_1}{L_{p,1}}\right)}{cosh\left(\frac{d_1}{L_{p,1}}\right) + \frac{S_p L_{p,1}}{D_{p,1}}sinh\left(\frac{d_1}{L_{p,1}}\right)}\right)\left(e^{\frac{V}{V_T}} - 1\right) \tag{2.80}$$

$$J_p^{\text{Photo}} = \int_0^{+\infty} F_p\left[\frac{\frac{\partial z_p}{\partial x}|_{x=0} - \frac{S_p}{D_{p,1}}z_p(\lambda,0)}{cosh\left(\frac{d_1}{L_{p,1}}\right) + \frac{S_p L_{p,1}}{D_{p,1}}sinh\left(\frac{d_1}{L_{p,1}}\right)} + \frac{r_p}{L_{p,1}}z_p(\lambda,d_1) - \frac{\partial z_p}{\partial x}|_{x=d_1}\right]d\lambda \tag{2.81}$$

where:

$$F_p = \frac{q\Phi_0 T_f^{\text{Top}} L_{p,1}^2 \alpha_1}{1 + R_b^{\text{Top}} R_f^{\text{Top}} e^{-2\alpha_1 d_E} - 2e^{-\alpha_1 d_E} Re\left(r_b^{\text{Top}} r_f^{\text{Top}} e^{-j\beta_1 d_E}\right)} \tag{2.82}$$

$$z_p = \frac{e^{-\alpha_1 x}}{1-(\alpha_1 L_{p,1})^2} + \frac{R_b^{\text{Top}} e^{-2\alpha_1 d_E} e^{\alpha_1 x}}{1-(\alpha_1 L_{p,1})^2} + \frac{2e^{-\alpha_1 d_E}}{1+(\beta_1 L_{p,1})^2} Re\left(r_b^{\text{Top}} e^{-j\beta_1 d_E} e^{j\beta_1 x}\right) \tag{2.83}$$

$$r_p = \frac{sinh\left(\frac{d_1}{L_{p,1}}\right) + \frac{S_p L_{p,1}}{D_{p,1}} cosh\left(\frac{d_1}{L_{p,1}}\right)}{cosh\left(\frac{d_1}{L_{p,1}}\right) + \frac{S_p L_{p,1}}{D_{p,1}} sinh\left(\frac{d_1}{L_{p,1}}\right)} \tag{2.84}$$

- p-QNR:

$$J_n^{\text{Tot}} = J_n^{\text{Photo}} + J_n^{\text{Dark}} \tag{2.85}$$

where:

$$J_n^{\text{Dark}} = -\left(\frac{qD_{n,2} n_{i,2}^2}{L_{n,2} N_D} \frac{sinh\left(\frac{d_2}{L_{n,2}}\right) + \frac{S_n L_{n,2}}{D_{n,2}} cosh\left(\frac{d_2}{L_{n,2}}\right)}{cosh\left(\frac{d_2}{L_{n,2}}\right) + \frac{S_n L_{n,2}}{D_{n,2}} sinh\left(\frac{d_2}{L_{n,2}}\right)}\right)\left(e^{\frac{V}{V_T}} - 1\right) \tag{2.86}$$

$$J_n^{\text{Photo}} = \int_0^{+\infty} F_n \left[-\frac{\frac{\partial z_n}{\partial x}|_{x=L} + \frac{S_n}{D_{n,2}} z_n(\lambda, L)}{cosh\left(\frac{d_2}{L_{n,2}}\right) + \frac{S_n L_{n,2}}{D_{n,2}} sinh\left(\frac{d_2}{L_{n,2}}\right)} + \frac{r_n}{L_{n,2}} z_n(\lambda, x_p) + \frac{\partial z_n}{\partial x}|_{x=x_p}\right] d\lambda \tag{2.87}$$

where:

$$F_n = \frac{q\Phi_0 T_f^{\text{Bot}} L_{n,2}^2 \alpha_2}{1 + R_b^{\text{Bot}} R_f^{\text{Bot}} e^{-2\alpha_2 d_B} - 2e^{-\alpha_2 d_B} Re\left(r_b^{\text{Bot}} r_f^{\text{Bot}} e^{-j\beta_2 d_B}\right)} \tag{2.88}$$

$$z_n = \frac{e^{-\alpha_2 x}}{1-(\alpha_2 L_{n,2})^2} + \frac{R_b^{\text{Bot}} e^{-2\alpha_2 d_B} e^{\alpha_2 x}}{1-(\alpha_2 L_{n,2})^2} + \frac{2e^{-\alpha_2 d_B}}{1+(\beta_2 L_{n,2})^2} Re\left(r_b^{\text{Bot}} e^{-j\beta_2 d_B} e^{j\beta_2 x}\right) \tag{2.89}$$

$$r_n = \frac{sinh\left(\frac{d_2}{L_{n,2}}\right) + \frac{S_n L_{n,2}}{D_{n,2}} cosh\left(\frac{d_2}{L_{n,2}}\right)}{cosh\left(\frac{d_2}{L_{n,2}}\right) + \frac{S_n L_{n,2}}{D_{n,2}} sinh\left(\frac{d_2}{L_{n,2}}\right)} \tag{2.90}$$

- SCR:

$$J_W^{Tot} = J_W^{\text{Photo}} = \int_0^{+\infty} q\Phi_0 \left[a_W + b_W\right] d\lambda \tag{2.91}$$

where:

$$a_W = \left[T_f^{\text{Top}} \frac{e^{-\alpha_1 d_1}\left(1 - e^{-\alpha_1 x_n}\right) + R_b e^{-\alpha_1 (d_E + x_n)}\left(e^{\alpha_1 x_n} - 1\right) + 2\frac{\alpha_1}{\beta_1} e^{-\alpha_1 d_E} Im\left(r_b\left(1 - e^{-j\beta_1 x_n}\right)\right)}{1 + R_b^{\text{Top}} R_f^{\text{Top}} e^{-2\alpha_1 d_E} - 2e^{-\alpha_1 d_E} Re\left(r_b^{\text{Top}} r_f^{\text{Top}} e^{-j\beta_1 d_E}\right)}\right] \tag{2.92}$$

$$b_W = \left[T_f^{\text{Bot}} \frac{\left(1 - e^{-\alpha_2 x_p}\right) + R_b e^{-2}\left(e^{\alpha_2 x_p} - 1\right) + 2\frac{\alpha_2}{\beta_2} e^{-\alpha_2 d_B} Im\left(r_b e^{-j\beta_2 d_2}\left(1 - e^{-j\beta_2 x_p}\right)\right)}{1 + R_b^{\text{Bot}} R_f^{\text{Bot}} e^{-2\alpha_2 d_B} - 2e^{-\alpha_2 d_B} Re\left(r_b^{\text{Bot}} r_f^{\text{Bot}} e^{-j\beta_2 d_B}\right)}\right] \tag{2.93}$$

It is worth noticing that J_p^{Dark} and J_n^{Dark} are propotional to $n_{i,1}^2$ and $n_{i,2}^2$ respectively: for this reason the dark current contributions of the two quasi neutral regions can be very different having materials with different n_i^2.

2.3.4 Photon-Recycling Factor

The Photon-Recycling Factor is now computed for the n-doped material and the p-doped material separately so that it can be written:

$$\tau_n^{\text{Rad}} = \frac{\left(1 - f_{pr}^{\text{Bot}}\right)}{BN_A} \tag{2.94}$$

$$\tau_p^{\text{Rad}} = \frac{\left(1 - f_{pr}^{\text{Top}}\right)}{BN_D} \tag{2.95}$$

2.4 Depleted Region and Perimeter Non-Radiative Recombination Dark Currents

In our treatise, it has been neglected the dark current's contribution relative to the perimeter non-radiative recombination due to the dangling bonds at the surface of the active material of the junction and, until now, the one relative to the non-radiative recombination in the SCR.
In order to derive an analytical model to describe these two contributions, a number of approximations are needed and the currently developed models are generally less reliable than the one for J_{01} (especially for $J_{Perimeter}$).
However, the perimeter current density contribution is usually negligible with respect to the others since it is to be multiplied by "$\left(\frac{Perimeter}{Area}\right)$" and, in commercial cells, this ratio is relatively very low. Furthermore, the model described in [6] has been used for homojunction simulations and the perimeter current density contribution has been always been negligible in the simulations. Finally, in the article's analysis strong approximations were needed. For these reasons, the perimeter current has been neglected in the simulations with heterojunctions.
As for the depleted region non-radiative dark current, the model described in [5] has been employed for the homojunctions while the one described in [8] has been employed for the heterojunctions:

- Homojunction:

$$J_{02} = -\alpha_{\text{asym}} K_B T n_i \left(\frac{1}{\tau_p^{\text{SRH}} \mathcal{E}_{\text{av}}} + \frac{1}{\tau_n^{\text{SRH}} \mathcal{E}_{\text{av}}} \right) \tag{2.96}$$

  with:

$$\alpha_{\text{asym}} = \frac{5}{8}\pi \tag{2.97}$$

$$\mathcal{E}_{\text{av}} = \frac{V_{\text{built-in}} - V}{W} \tag{2.98}$$

- Heterojunction:

$$J_{02} = \frac{-qW\sqrt{n_{i,1} n_{i,2}}}{\sqrt{\tau_{\text{p,eff}}^{\text{Non-Rad}} \tau_{\text{n,eff}}^{\text{Non-Rad}}}} \tag{2.99}$$

  with:

$$\tau_{\text{p,eff}}^{\text{Non-Rad}} = \left(\frac{1}{\tau_{p,1}^{\text{SRH}}} + \frac{1}{\frac{d_E^2}{\pi^2 D_{p,1}} + \frac{d_E}{S_{\text{int}}}} \right)^{-1} \tag{2.100}$$

$$\tau_{\text{n,eff}}^{\text{Non-Rad}} = \left(\frac{1}{\tau_{n,2}^{\text{SRH}}} + \frac{1}{\frac{d_B^2}{\pi^2 D_{n,2}} + \frac{d_B}{S_{\text{int}}}} \right)^{-1} \tag{2.101}$$

  S_{int}: surface recombination speed of the interface between the n-doped region and the p-doped region (in our case, between GaAs and InGaP). This interface is in the deep inside the SCR where there are always almost no minority carriers. Furthermore the measurements of the cells

to determine J_{01} have been carried out at a relatively high applied bias when the contribution of J_{02} is negligible. For these reasons, a fixed value for S_{int} taken from the "Ioffe" ([12]) website has been employed.

2.5 External Quantum Efficiency (EQE)

The external quantum efficiency (EQE) is defined as the ratio of the number of electron-hole pairs generated and collected over the number of photons impinging on the device at zero applied bias. It can be defined as:

$$EQE(\lambda) = \frac{\left(\frac{I^{\text{Photo}}(V=0)}{q}\right)}{\left(\frac{P_{\text{opt},0}(\lambda)}{E_{\text{photon}}(\lambda)}\right)} = \frac{I^{\text{Photo}}(V=0)}{Area * q\Phi_0(\lambda)} = \frac{J^{\text{Photo}}(V=0)}{q\Phi_0(\lambda)} \tag{2.102}$$

The EQE measurement is a fundamental tool to understand the performance of the cell at specific wavelengths.

2.6 Metal Coverage

Actual cells are characterized by the presence of metal contacts on the front side. While for EQE measurements a spot of the cell without coverage is illuminated, for I-V measurements the coverage affects the overall performance of the cell.
The developed model takes into account this fact by computing a weighted average of the reflectances and transmittances on the front side and of the photon-recycling factors given by the layers on top of cell without coverage and the ones with coverage only for the I-V characteristic simulations. In fact, among the input variables in the model there is the "*coverage*" which is defined as the percentage of the front side surface covered by the metal contacts.
Defining $R_{f,1}$ and $T_{f,1}$ as the normal front reflectance and transmittance considering the front layers with no coverage and $R_{f,2}$ and $T_{f,2}$ as the normal front reflectance and transmittance considering the front layers where the coverage is, the overall normal reflectances and transmittances are given by:

$$R_f = R_{f,1} * (1 - coverage) + R_{f,2} * coverage \tag{2.103}$$

$$T_f = T_{f,1} * (1 - coverage) + T_{f,2} * coverage \tag{2.104}$$

Furthermore, defining $f_{pr,1}$ as the photon-recycling factor computed considering the front layers with no coverage and $f_{pr,2}$ as the photon-recycling factor computed considering the front layers where the coverage is, the overall photon-recycling factor is given by:

$$f_{pr} = f_{pr,1} * (1 - coverage) + f_{pr,2} * coverage \tag{2.105}$$

3 | Experimental Set-Up

A series of substrate-based solar cells have been grown and processed both to test the validity of the theoretical model and to derive an empirical emitter doping-and-thickness dependent model for the front surface recombination speed.
This work has been focused on GaAs-InGaP abrupt heterojunctions. In fact, as mentioned at the end of sub-section 2.3.3, the dark current contributions of the two quasi neutral regions are heavily affected by n_i. For this reason, having $n_{\mathrm{i,GaAs}} \cong 2.1 * 10^6 \mathrm{cm}^{-3} >> n$

3.1 Processing

The processing consists in depositing the metal on the top and the bottom and etching the grown structure (with the metal) where it is not wanted, leaving it only where the solar cells will be. This is achieved thanks to photolithography.

First of all, the wafer is cleaned to remove the oxide and other impurities deposited on the top. Secondly, a negative photoresist is deposited on the front side and baked at 100°C in order to perform the photolithography. The wafer is then UV-illuminated for 40s and placed in a developing solution to remove only the not-illuminated photoresist.
A 200nm and 100nm thick layer of Gold are deposited through metal evaporation respectively at the top and at the bottom of the wafer. Using the metal lift-off technique, acetone is used to etch the remaining photoresist lifting off the Gold on top of it, leaving the metal only for the cells' contacts.
At this point, a positive photoresist is deposited, baked, illuminated and developed so that it is left only certain regions of the wafer. Through three selective etching processes, the 300nm GaAs n-contact, the 20nm AlInP window and the GaAs emitter are removed in the areas not protected by the positive photoresist leaving a set of cells with different areas (mostly $1\mathrm{cm}^2$ and $0.25\mathrm{cm}^2$).
Finally, the photoresist is removed using acetone again and the GaAs n-contact layer on the cells is etched using the metal contacts as masks.
The final structure can be seen in Fig.3.1 while a picture of an actual sample is in Fig.3.2.

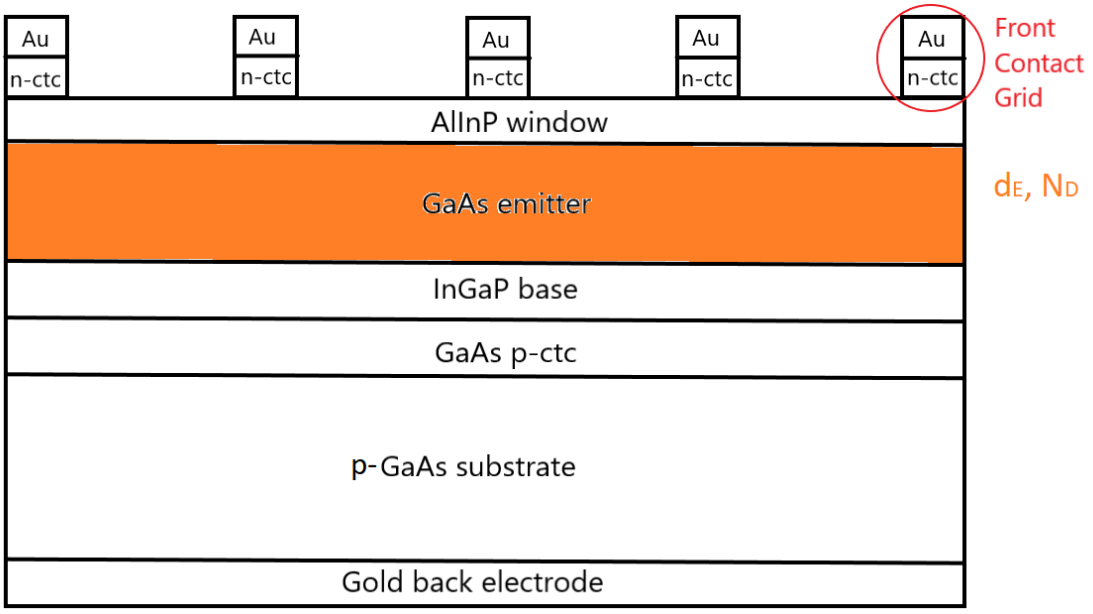

Figure 3.1: 2D schematic of the final structure

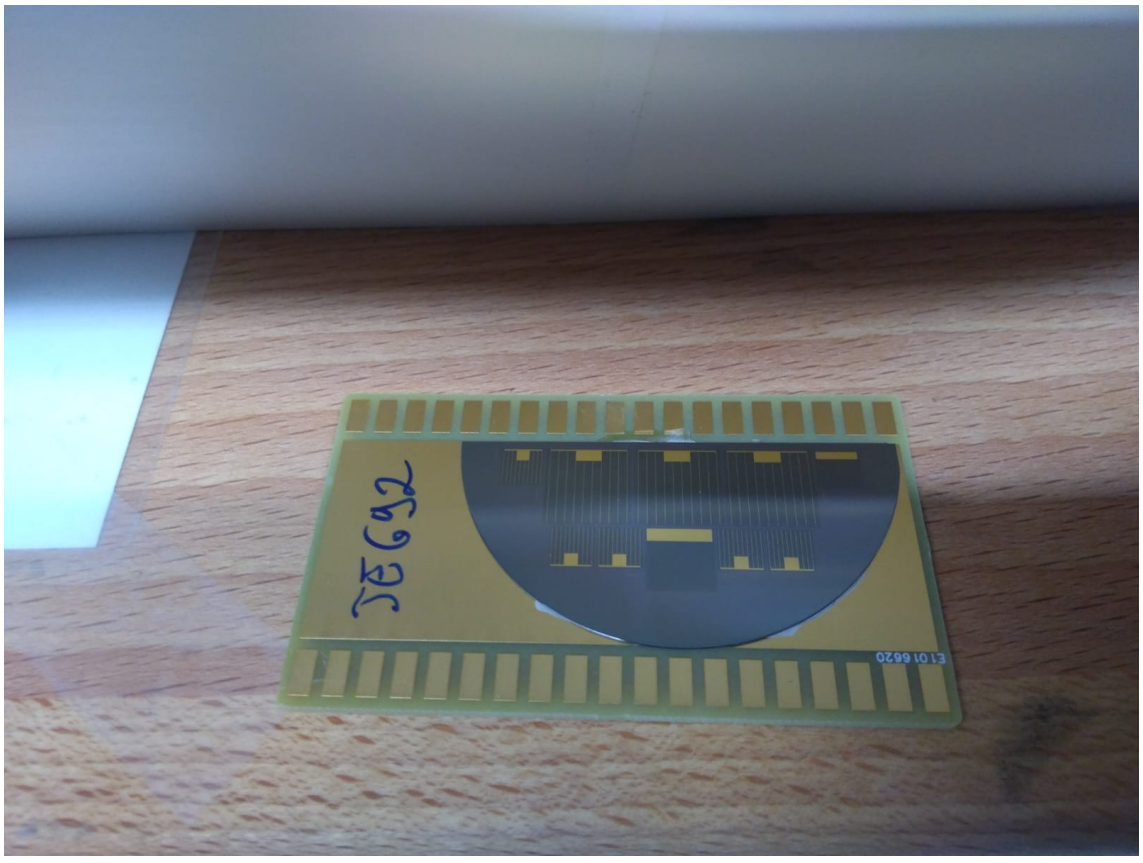

Figure 3.2: Processed half wafer with solar cells on it

3.2 Measurements

3.2.1 I-V characteristic

All the measurements are performed at 298.15K=25°C. The illumination is provided by a lamp generating a light which simulates the AM1.5G spectrum. Both the temperature and the illumination are controlled (and 'corrected' if needed) using a reference cell and a temperature sensor.
The dark current is normally measured varying the voltage bias applied keeping the cell in the dark. This is what is done under the condition that the output current is lower than 1mA for our cells (which usually implies that the voltage applied is below 1V). In fact, the parasitic series resistance of the top contact makes this method not effective for higher currents, heavily affecting the measurement. For this reason, in order to measure the I-V characteristic of the cell in the dark at higher voltages, the short-circuit current and the open-circuit voltage are measured under different illuminations. This is done since, under illumination at $V = V_{oc}$, the current is zero because $I^{\text{Dark}} = -I^{\text{Photo}}$. In this way, assuming that I^{Photo} is approximately constant changing the voltage applied, it is possible to measure the dark current at higher voltages without being affected by series parasitic resistances.
The different illuminations are obtained using progressively opaque glasses between the lamp and the cell.
From the dark I-V characteristic experimental data, it is possible to find values for J_{01} and J_{02} to plug into the theoretical model in order to fit the data. Using the obtained values of J_{01}, thanks to the fact that $J_{01} \cong J_{01,p}$ and that all the other parameters are defined, it is straightforward to find the value S_f that fit the J_{01} data for a specific voltage (in our case it was set $V = 1.055$V, because the data relevant to find J_{01} were around this voltage). Through the simulations, it has been checked that changing the voltage applied of ± 10mV the absolute values of fitted surface recombination speeds change less than 0.5ms^{-1}.
The uncertainty over J_{01} is $\cong \pm 0.1 \times 10^{-20}\text{Acm}^{-2}$ which leads the uncertainty over S_f to be $\cong \pm 1\text{ms}^{-1}$. This has been also tested with the support of simulations.

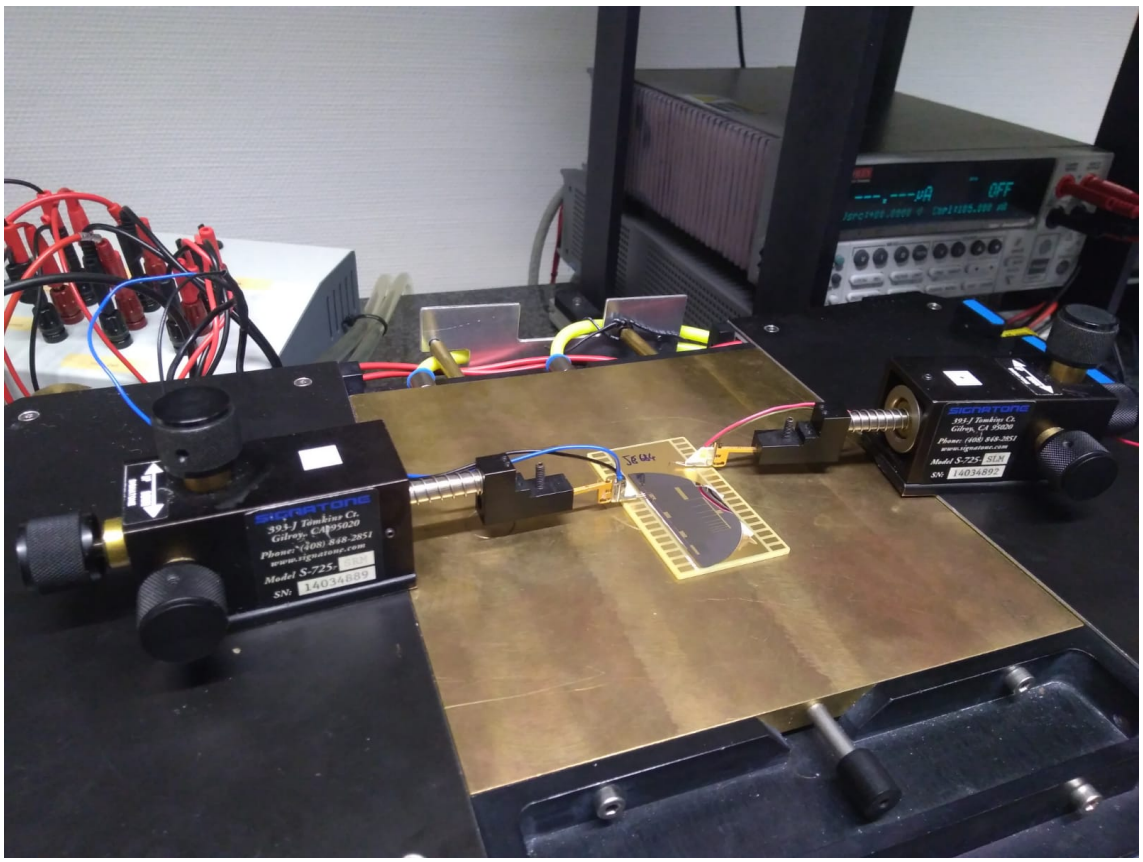

Figure 3.3: Dark current measurement set-up

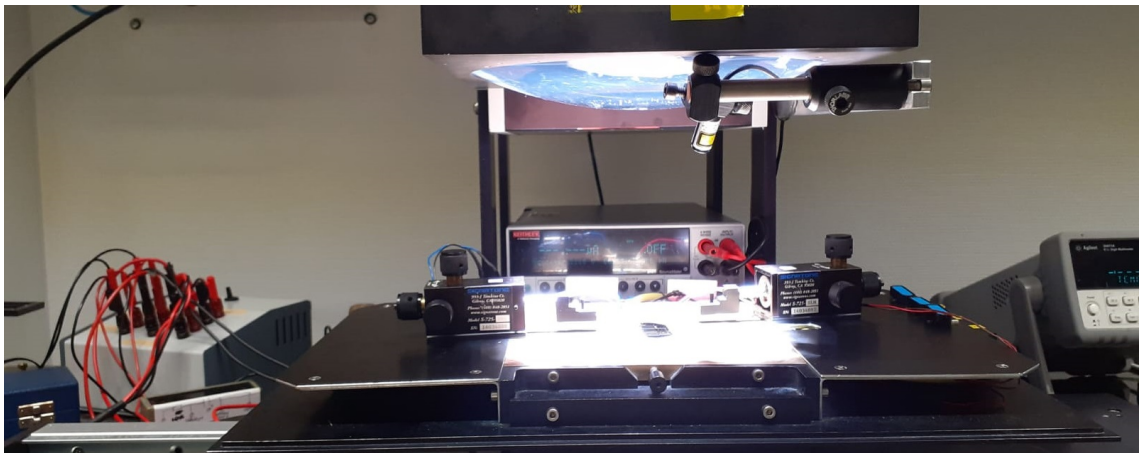

Figure 3.4: Illumination characteristic measurement set-up

3.2.2 External Quantum Efficiency (EQE)

The EQE is measured illuminating the cell with a light source at specific wavelengths, in a region without coverage. The generated short-circuit current is measured at zero applied bias and, knowing Φ_0 and the illuminated area, through Eq.2.102, the EQE is computed for each wavelength.
The light source is not continuous: its amplitude oscillates at a specific frequency. The output current

from the cell is put through a lock-in amplifier which filters out the DC component leaving only the short-circuit current due to the light source and not to light noise. In this way, the J_{sc} generated is linked to specific wavelengths.
Moreover, the EQEs have been scaled using the measured short-circuit currents. The EQE for each wavelength is scaled considering that its product with the lamp photon-flux and the elementary charge, integrated over all the wavelengths, must give back, as a result, the measured J_{sc}.

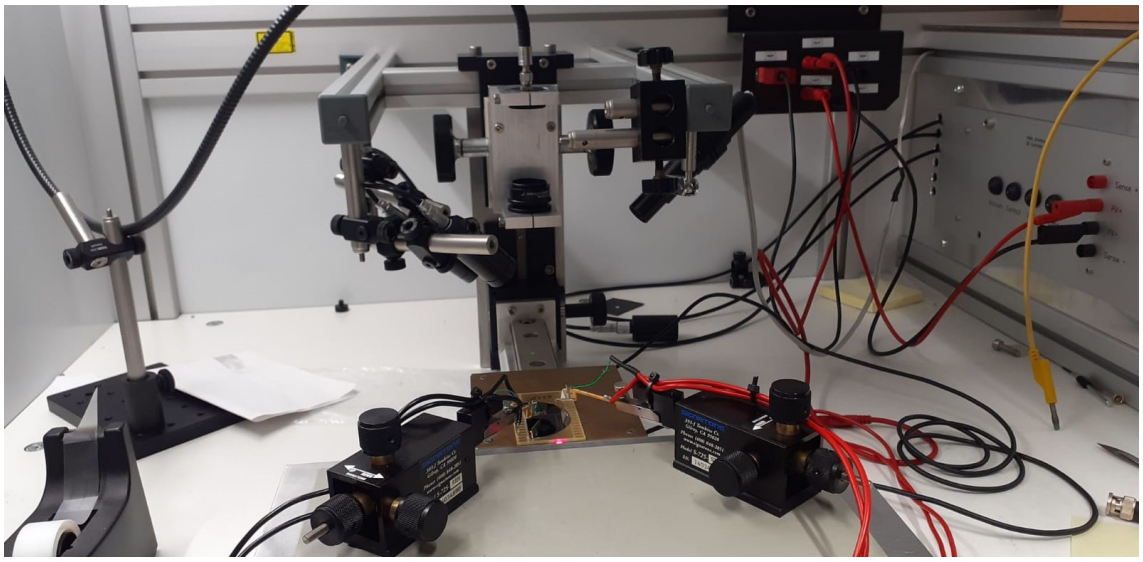

Figure 3.5: External Quantum Efficiency measurement set-up

4 | Experimental Results

A series of similar substrate GaAs-InGaP heterojunction solar cells with different emitter thicknesses and doping levels were grown, processed and measured.
All the cells are characterized by a 100nm thick and $5\times10^{17}\text{cm}^{-3}$ p-doped InGaP region. Furthermore, as can be seen from Fig.**??**, the top layers without metal coverage consist only of a 20nm thick AlInP layer while, the regions with metal coverage, have, on top of the AlInP layer, a 300nm GaAs layer and a 200nm Au layer. The percentage of the front surface covered by the metal contacts is 8%.

4.1 Variable Emitter Doping

The first important result was given by two sets of four cells, which differ only by the emitter doping level. The n-doped GaAs active region thickness is kept constant at 300nm. The cells of the first set have a uniform doping level while the ones of the second set are characterized by a 10nm GaAs layer of a $5 \times 10^{15}\text{cm}^{-3}$ constant doping density at the interface between the GaAs emitter and the AlInP window. The results can be observed in Fig.4.1.

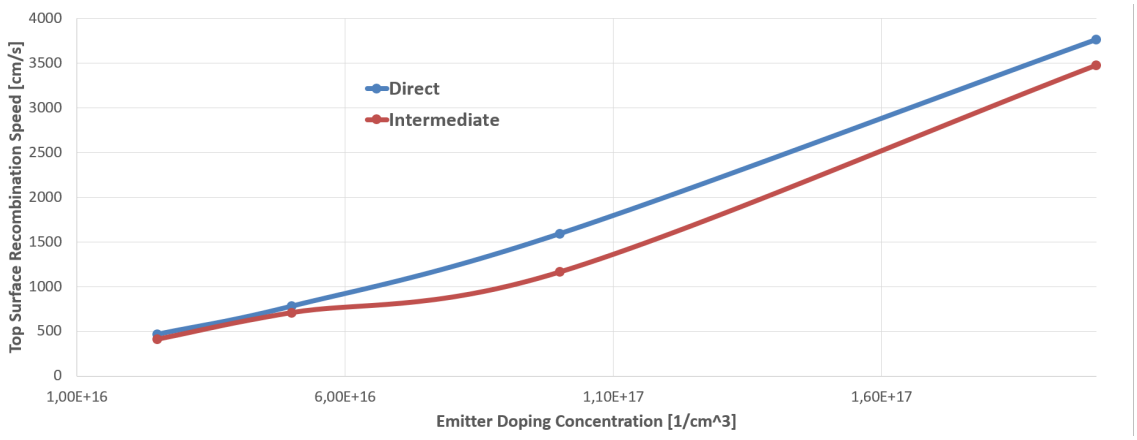

Figure 4.1: Derived S_f values for different emitter doping levels. In blue, the set of cells without intermediate layer and, in red, the set of cells with constant-doping intermediate layer

As expected, the set of cells with intermediate layer is performing better with lower S_f values. This can be explained by considering that higher doping levels lead to a higher number of impurities and recombination centers at the GaAs-AlInP interface, hence to a higher surface recombination speed.
The most important result, however, consists in the fact that the surface recombination speed is increasing with the doping levels in both cases. As mentioned before, the assumption was that the surface recombination speed value would depend on the excess minority carriers at the interface other than on the interface quality. From Fig.4.1, it is clear that, assuming the same interface quality, changing only the emitter doping levels and hence the amount of minority carriers at the GaAs-AlInP interface, we have different S_f values. The assumption of approximately the same interface quality

is definitely reasonable since, for the cells with intermediate layer, both the doping levels and growth methods of the emitter-window interface have been identical for all the cells.
It is known that, increasing the doping level, the excess minority carriers decreases, hence p'_{int} decreases. For this reason, it appears that, decreasing the amount of minority carriers at the interface, the surface recombination speed increases. One possible explanation could be that, increasing p'_{int}, the recombination centers at the interface might saturate, leading to lower S_f values.
For lower doping levels, the intermediate, lower doped, GaAs layer between the emitter and the window provides a decrease of the front surface recombination speed of approximately 10%.

4.2 Variable Emitter Thickness

Four more sets of cells have been grown, processed and measured. Each set is characterized by a constant emitter doping level. The emitter thickness has been varied between 0.3um and 2.7um.
Knowing, for each doping level, the n-doped quasi-neutral region thickness (n-QNR) ($d_1 = d_E - x_n$), the values of the fitted surface recombination speed, the measured open-circuit voltages and short-circuit currents relative to the n-QNR thicknesses are plotted in Fig.4.2, Fig.4.3 and Fig.4.4, respectively.

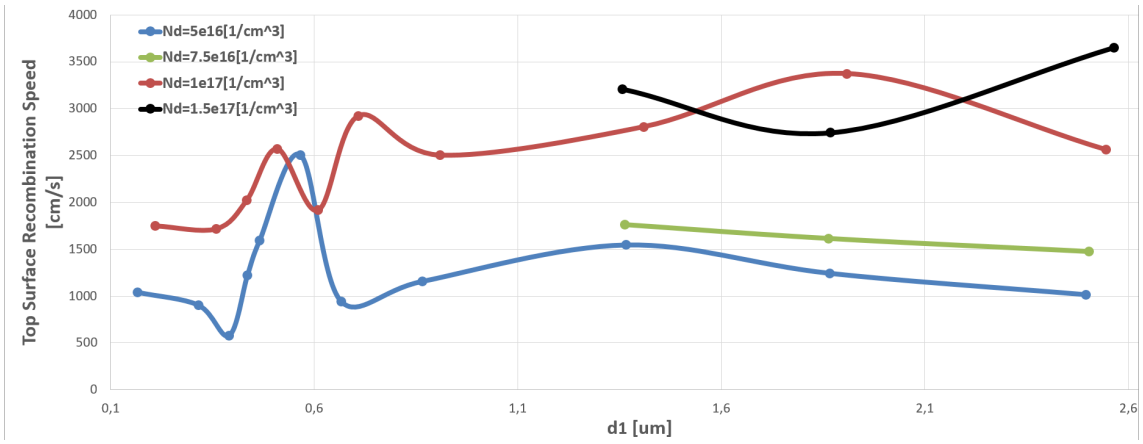

Figure 4.2: Derived S_f values for different n-QNR thicknesses. In blue, the set of cells with $N_D = 5 \times 10^{16}\text{cm}^{-3}$; in green, the set of cells with $N_D = 7.5 \times 10^{16}\text{cm}^{-3}$; in red, the set of cells with $N_D = 1 \times 10^{17}\text{cm}^{-3}$; in black, the set of cells with $N_D = 1.5 \times 10^{17}\text{cm}^{-3}$

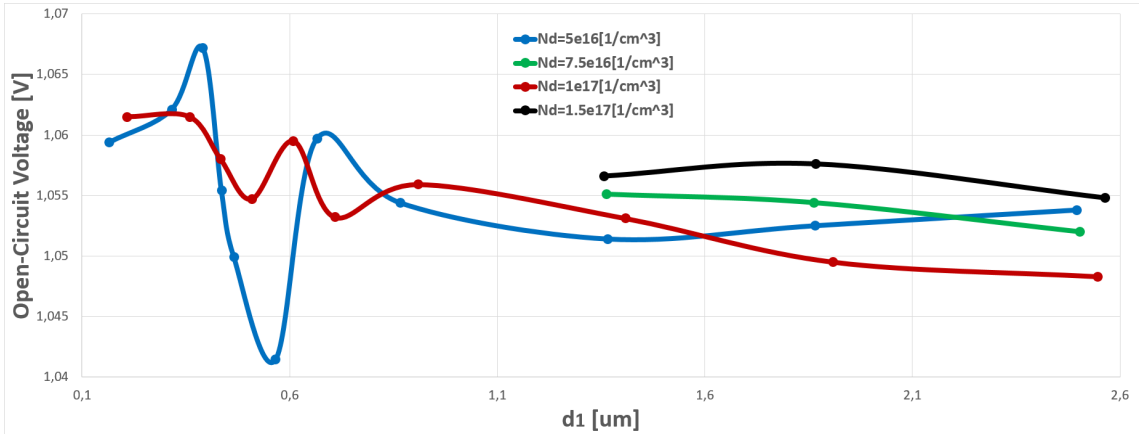

Figure 4.3: Measured V_{oc} values for different n-QNR thicknesses. In blue, the set of cells with $N_D = 5 \times 10^{16}\text{cm}^{-3}$; in green, the set of cells with $N_D = 7.5 \times 10^{16}\text{cm}^{-3}$; in red, the set of cells with $N_D = 1 \times 10^{17}\text{cm}^{-3}$; in black, the set of cells with $N_D = 1.5 \times 10^{17}\text{cm}^{-3}$

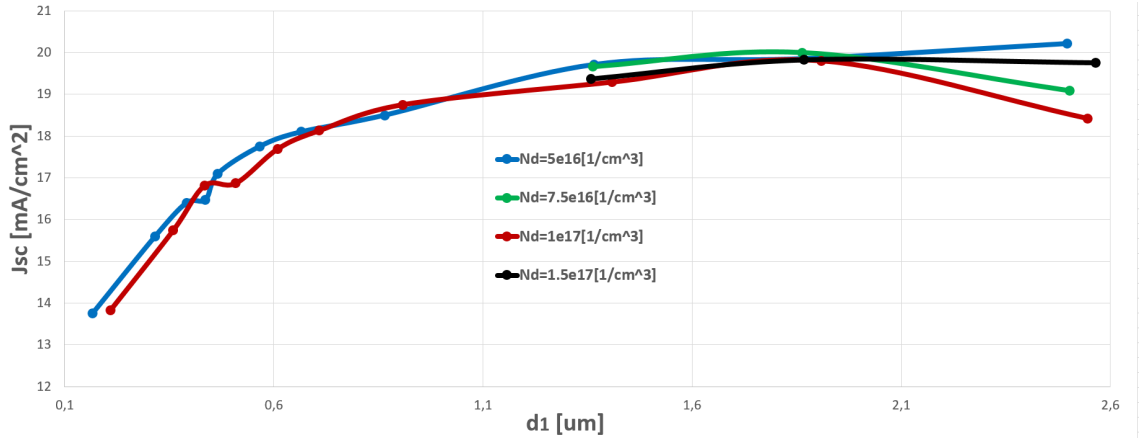

Figure 4.4: Measured J_{sc} values for different n-QNR thicknesses. In blue, the set of cells with $N_D = 5 \times 10^{16}\text{cm}^{-3}$; in green, the set of cells with $N_D = 7.5 \times 10^{16}\text{cm}^{-3}$; in red, the set of cells with $N_D = 1 \times 10^{17}\text{cm}^{-3}$; in black, the set of cells with $N_D = 1.5 \times 10^{17}\text{cm}^{-3}$

Looking at the measured J_{sc}, the results appear to be consistent with the expectations. In fact, increasing the emitter thickness, the short-circuit current increases gradually until it reaches its maximum value. For higher values of d_1 and higher N_D, the current slightly decreases. This is due to the fact that less holes are collected at the n-contact at the top of the cells. The emitter thickness at which there is the J_{sc} maximum decreases increasing the doping levels. This is explained considering that, for higher N_D values, the hole mobility and lifetime get worse causing a decrease of the hole diffusion length in the GaAs n-doped quasi-neutral region.
Fig.4.2 provides another indication that, maintaining the same parameters in the interface growth (same doping levels and same growth method), different surface recombination speed values are fitted for different values of excess minority carriers at the interface.
Still looking at Fig.4.2, considering the relation between S_f and d_1, it is clear that, for relatively low emitter thicknesses, the $S_f = S_f(d_1)$ function is not monotonic. Both for the $N_D = 5 \times 10^{16}\text{cm}^{-3}$ and the $N_D = 1 \times 10^{17}\text{cm}^{-3}$ curves, two troughs and two peaks are present for relatively thin emitters. Since the same behaviour can be observed in a direct measurement such as V_{oc} (Fig.4.3), the derivation of the S_f values is not subjected to gross mistakes.

Regarding higher d_1 values, the behaviour is monotonic-decreasing for the $N_D = 5 \times 10^{16}\text{cm}^{-3}$ and the $N_D = 7.5 \times 10^{16}\text{cm}^{-3}$ curves (Fig.4.2), while it appears more random for higher doping levels. However, this could be related to the oscillatory behaviour at shorter emitter thicknesses. In fact, the peak for the $N_D = 1 \times 10^{17}\text{cm}^{-3}$ curve is slightly shifted from the $N_D = 5 \times 10^{16}\text{cm}^{-3}$ curve: what we see for higher emitter thicknesses and doping levels, is likely given by other peaks and troughs due to the same oscillatory behaviour seen for thinner emitters.
This oscillatory nature of the $S_f = S_f(d_1)$ function led to think of an optical effect (interference), affecting the excess minority carriers at the interface. However, this theory is challenged by the shift in the oscillations for different doping levels. Furthermore, this behaviour is unlikely to be the effect of the photon-recycling since, otherwise, we would have expected a monotonic function.
The fact that, for lower doping levels and at higher emitter thicknesses, the surface recombination speed decreases with increasing d_1, is in contrast with what has been found in section 4.1. In fact, increasing d_1, the excess minority carriers at the emitter-window interface is intuitively expected to decrease. This is the opposite of what has been found in the first two sets of cells in which the only changing variable was the emitter doping level. It is, however, important to notice that, this decreasing trend is only local: this behaviour could just be given by oscillations with a larger period.
Furthermore, it might be useful to look at the theory. Solving Eq.9.1, the excess minority carriers in the emitter is derived and, setting $x = 0$, the analytical expression for $p'_{\text{int}} = p'_{\text{int,Dark}} + p'_{\text{int,Photo}}$ is obtained:

$$p'_{\text{int,Dark}} = \left(\frac{1}{\cosh\left(\frac{d_1}{L_{p,1}}\right) + \left(\frac{S_p L_{p,1}}{D_{p,1}}\right) \sinh\left(\frac{d_1}{L_{p,1}}\right)} \right) \frac{n_i^2}{N_D} \left(e^{\left(\frac{V}{V_T}\right)} - 1 \right) \tag{4.1}$$

$$p'_{\text{int,Photo}} = \int_0^{+\infty} F'_p \left[Factor_1 + Factor_2 \right] d\lambda \tag{4.2}$$

where:

$$F'_p = \frac{\Phi_0 T_f^{\text{Top}} L_{p,1}^2 \alpha_1}{2D_p \left(1 + R_b^{\text{Top}} R_f^{\text{Top}} e^{-2\alpha_1 d_E} - 2e^{-\alpha_1 d_E} Re\left(r_b^{\text{Top}} r_f^{\text{Top}} e^{-j\beta_1 d_E}\right)\right)} \tag{4.3}$$

$$Factor_1 = \frac{\sinh\left(\frac{d_1}{L_{p,1}}\right) \left[L_p \frac{\partial z_p}{\partial x}|_{x=0} + \left(1 + \frac{S_p L_{p,1}}{D_{p,1}}\right) z_p(\lambda, d_1) e^{\left(\frac{d_1}{L_{p,1}}\right)} - \frac{S_p L_{p,1}}{D_{p,1}} z_p(\lambda, 0) \right]}{\left[\cosh\left(\frac{d_1}{L_{p,1}}\right) + \frac{S_p L_{p,1}}{D_{p,1}} \sinh\left(\frac{d_1}{L_{p,1}}\right) \right]} \tag{4.4}$$

$$Factor_2 = z_p(\lambda, 0) - e^{\left(\frac{d_1}{L_{p,1}}\right)} z_p(\lambda, d_1) \tag{4.5}$$

The emitter doping level appears only in the expression for the excess minority carriers at the interface in dark: $p'_{\text{int,Dark}} \propto \frac{1}{N_D}$. On the other hand, d_1 affects both $p'_{\text{int,Dark}}$ and $p'_{\text{int,Photo}}$. In the expression for $p'_{\text{int,Dark}}$, the dependency is only on the ratio $\left(\frac{d_1}{L_p}\right)$, while, in $p'_{\text{int,Photo}}$, is also on the product (α_1). Both these factors appear as exponential arguments. As described before, the theoretical hole diffusion length in the GaAs emitter depends on multiple factors. However, in all of the considered cells, it always holds: $d_1 << L_p$. For this reason, measuring higher emitter thickness cells is likely to be essential in understanding the general behaviour of the $S_f = S_f(d_1)$ function and, ultimately, the relation between the surface recombination speed and the excess minority carriers at the interface.

4.3 Data-Simulations Comparison

Using the extrapolated S_f and J_{02} values, through the theoretical model, the measured V_{oc}, J_{sc} and EQEs have been compared with the simulated ones.

All the simulations have been run considering the wavelengths between 300nm and 900nm with a spacing of 1nm.

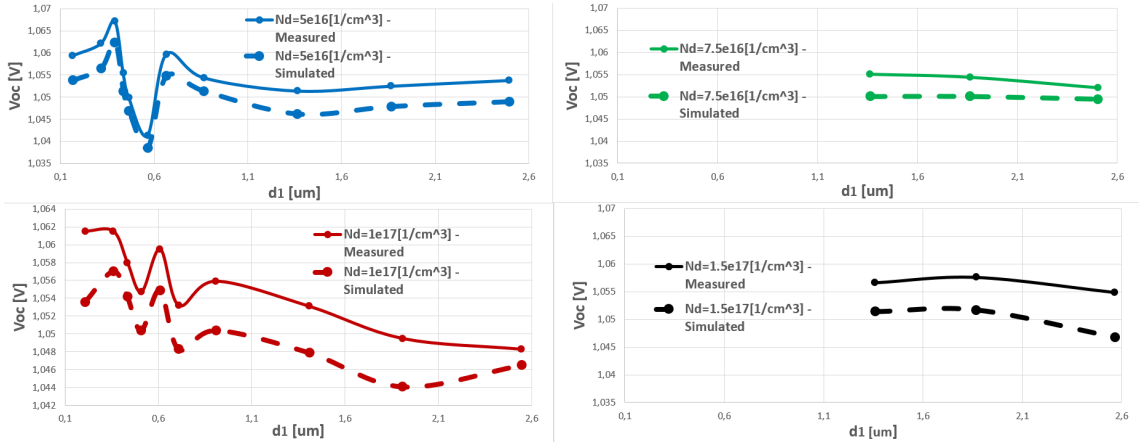

Figure 4.5: Measured vs simulated V_{oc} values for different n-QNR thicknesses. The continuous lines are the experimental ones and the dashed lines are the theoretical ones. In blue, the set of cells with $N_D = 5 \times 10^{16}\text{cm}^{-3}$; in green, the set of cells with $N_D = 7.5 \times 10^{16}\text{cm}^{-3}$; in red, the set of cells with $N_D = 1 \times 10^{17}\text{cm}^{-3}$; in black, the set of cells with $N_D = 1.5 \times 10^{17}\text{cm}^{-3}$

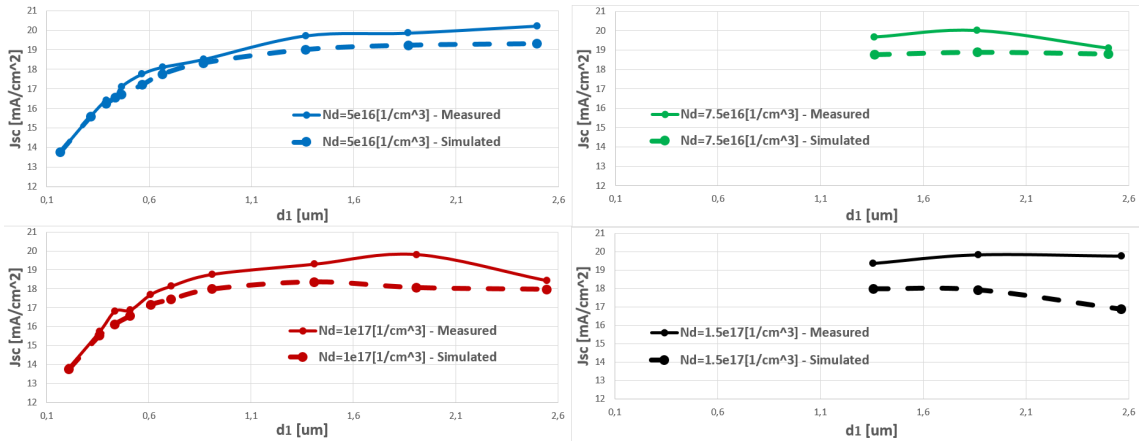

Figure 4.6: Measured vs simulated J_{sc} values for different n-QNR thicknesses. The continuous lines are the experimental ones and the dashed lines are the theoretical ones. In blue, the set of cells with $N_D = 5 \times 10^{16}\text{cm}^{-3}$; in green, the set of cells with $N_D = 7.5 \times 10^{16}\text{cm}^{-3}$; in red, the set of cells with $N_D = 1 \times 10^{17}\text{cm}^{-3}$; in black, the set of cells with $N_D = 1.5 \times 10^{17}\text{cm}^{-3}$

From Fig.4.5, it is clear that the model is constantly slightly underestimating the open-circuit voltage for each thickness and doping level. Furthermore, looking at Fig.4.6, it is clear that for higher emitter thicknesses the modelled short-circuit current density is underestimated too.
To better compare the model with the experiments and understand the nature of the differences, the external quantum efficiencies have been measured for most cells with $N_D = 5 \times 10^{16}\text{cm}^{-3}$ and $N_D = 1 \times 10^{17}\text{cm}^{-3}$. Some of the results have been plotted with the simulated EQEs.

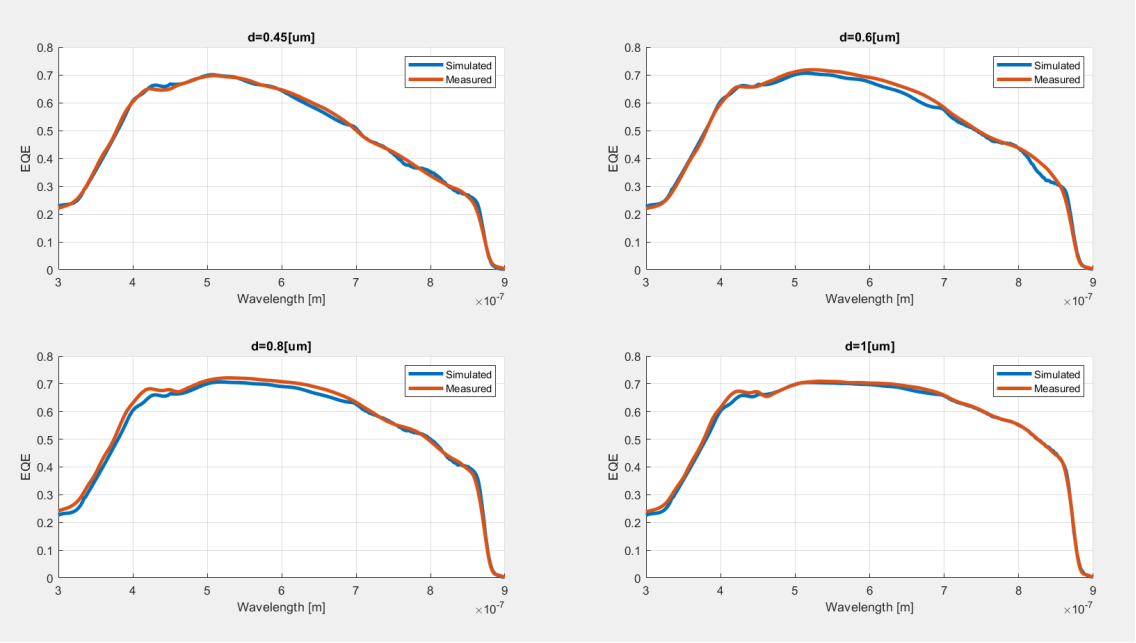

Figure 4.7: Measured vs simulated EQEs for $N_D = 5 \times 10^{16}\text{cm}^{-3}$. The red lines are the experimental ones and the blue lines are the theoretical ones

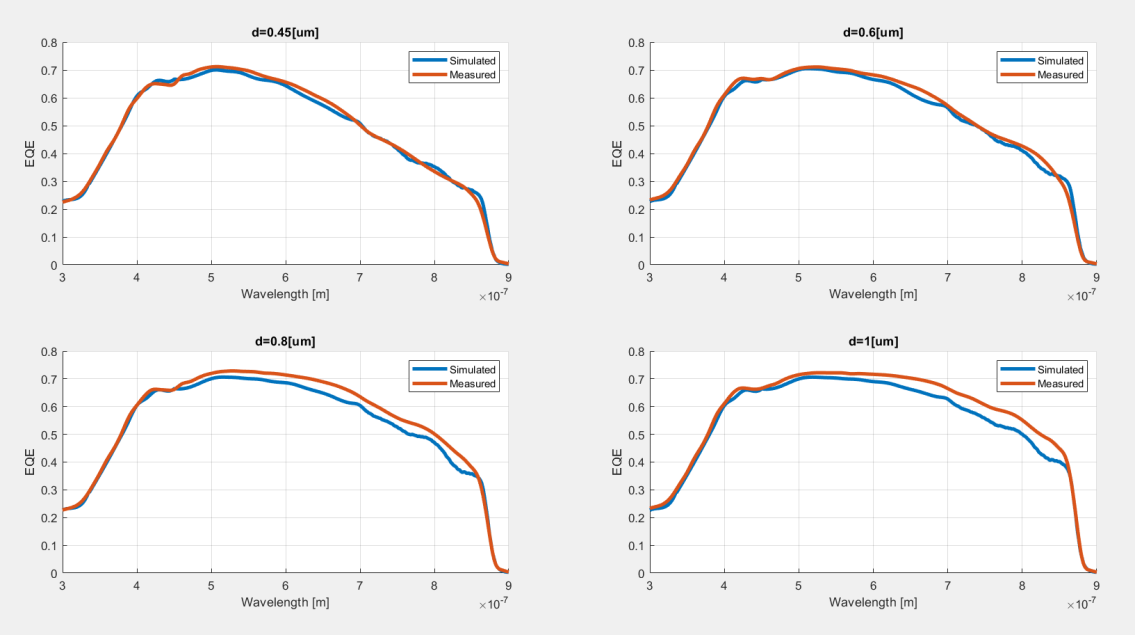

Figure 4.8: Measured vs simulated EQEs for $N_D = 1 \times 10^{17}\text{cm}^{-3}$. The red lines are the experimental ones and the blue lines are the theoretical ones

From Fig.4.7 and Fig.4.8, it is clear that the model is a very good fit for smaller emitter thickness cells and lower doping levels, while it starts to underestimate the EQE at "central" wavelengths for higher d_1 values. This explains the lower theoretical short-circuit current densities for higher emitter thicknesses and doping levels. At first, an underestimation of the hole diffusion length in the GaAs emitter was thought to be the cause of the problem. However, the simulations were run with higher

L_p values with the same results. To this moment, the reason for the underestimation of the EQEs at higher emitter thicknesses is unknown.
In general, it is very important to notice that the correct definition of the materials complex refractive indexes is fundamental to obtain precise results. In this study, different indexes found on different databases have been used to describe optically the active materials and the AlInP-window. The simulations results have been very different for each combination of the found data.

5 | Optimization

A Matlab routine has been developed in order to determine which are the best solar cell structures in terms of actual maximum power produced according to the model. The maximum electrical power is derived computing the total current $\left(I^{\text{Tot}} = I^{\text{Photo}} + I^{\text{Dark}}\right)$ for each applied voltage V and extracting the maximum value of the product $P_{\text{el}} = I^{\text{Tot}} \times V$.
Substrate-based solar cells are characterized by the presence of a highly doped substrate between the p-contact layer and the back metal contact. In order to increase the photon-recycling and improve the overall efficiency, thin-film solar cells are generally used to obtain the highest output features. Due to the much easier processing, for the surface recombination speed investigation, substrate-based heterojunctions have been used; however, for the optimization, it was decided to use a thin-film cell to maximize the performances. The back contact is a planar Au layer (not textured). The simulated structure can be seen in Fig.5.1.
Furthermore, based on the results of the two sets of cells with different emitter doping levels, a low doped 10$[nm]$ thick intermediate GaAs layer between the emitter and the window was grown so to achieve the lowest surface recombination speed possible.

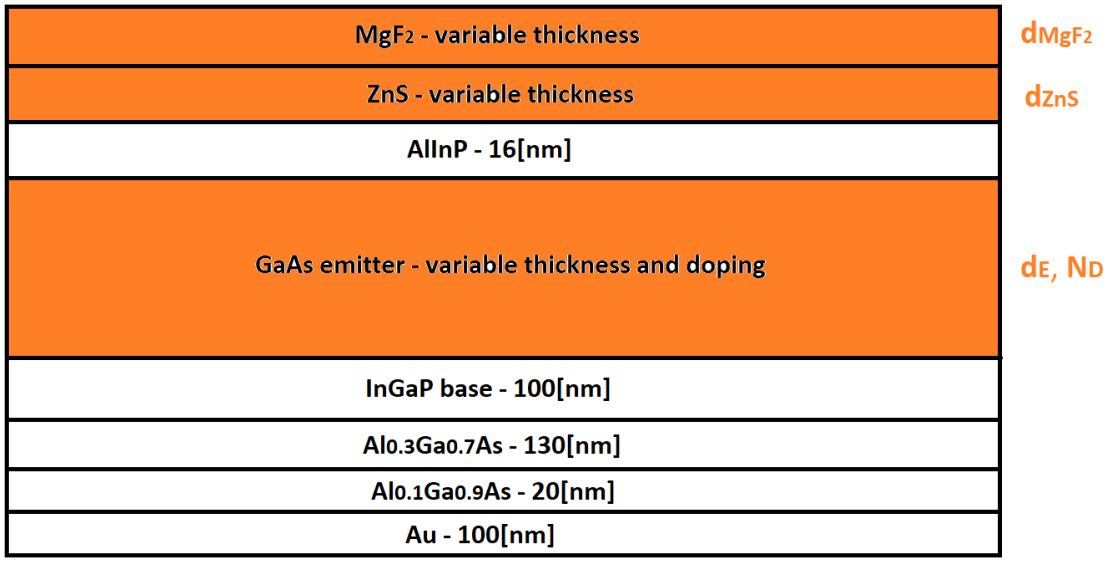

Figure 5.1: 2D schematic of the simulated thin-film cell

Two optimizations of a thin-film GaAs-InGaP heterojunction solar cell were performed. The first on the emitter thickness and doping level and, using the results of this one, a second optimization routine was run on the anti-reflection coating (ARC) thicknesses (d_{MgF_2} and d_{ZnS}). The ARC consists in, starting from the top, a layer of MgF_2 and a layer of ZnS and it is used to enhance the transmittance of the light from the top of the cell to the active region. Of course, in the routine, while different

combinations of the variables are simulated, the other cells parameters are kept constant.
In order for the optimization program to work, every parameter has to be defined for each of the combinations of the variables. In Ch.(2) all the parameters have been defined through analytical expressions except for the minority carrier SRH lifetimes, the mobilities and the surface recombination speeds. As mentioned in the introduction, empirical doping-and-temperature dependent models for the GaAs SRH lifetimes and mobilities have been derived in [1] and [2]. As for the GaAs emitter - AlInP window surface recombination speed, an emitter thickness and doping dependent model has been derived using the collected experimental data for the regions: 1.4um$<d_E<$2.6um and $5 \times 10^{16}\text{cm}^{-3}<N_D<1.5 \times 10^{17}\text{cm}^{-3}$. For this purpose, a cubic 2D Matlab interpolation has been used. Finally, for the InGaP base, constant values for the SRH lifetimes, the mobilities found in the online semiconductor database "Ioffe" ([12]) have been used, while, for the InGaP base - AlGaAs p-contact bottom surface recombination speed, a constant value of 20ms^{-1} has been set. These approximations are allowed since the current contributions given by the InGaP part of the active region are negligible with respect to the ones given by the GaAs part of the active region.
As mentioned in section 4.3, it is important to notice again that, according to the complex refractive indexes used, the results vary quite sensibly. Furthermore, the results are also different according to the interpolation method used to derive the empirical $S_f = S_f(d_E, N_D)$ function.
One of the optimization routines results can be observed in Fig.5.2 and 5.3.

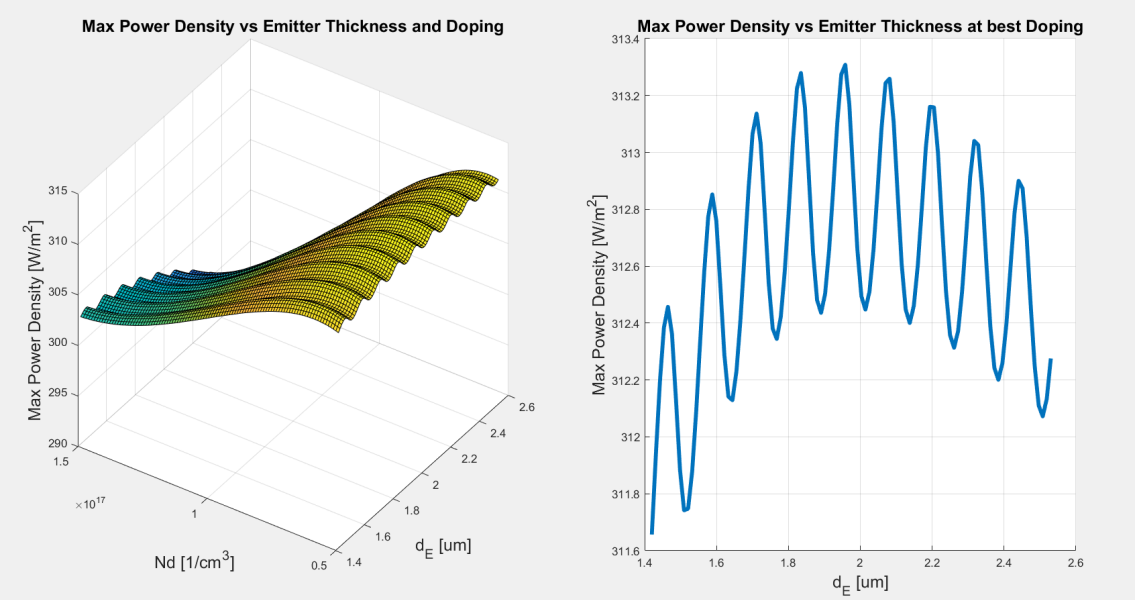

Figure 5.2: Simulated maximum power density vs emitter thickness and doping level

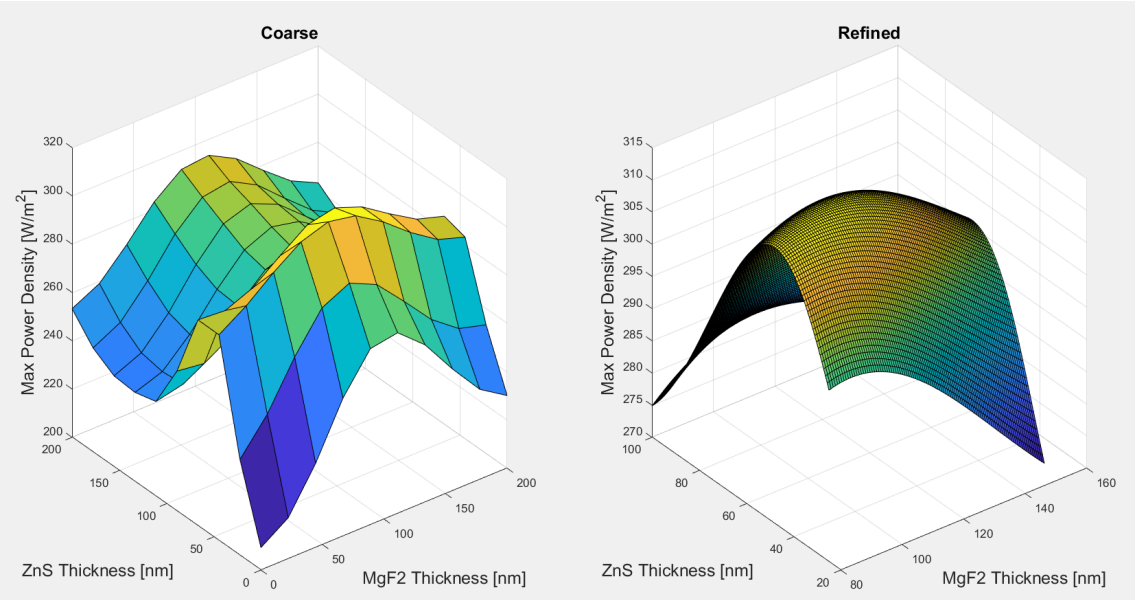

Figure 5.3: Simulated maximum power density vs MgF_2 layer and ZnS layer thicknesses

The oscillatory behaviour of the theoretical maximum power over the emitter thickness in Fig.5.2 is due to the light interference. In fact, the considered emitter thicknesses are comparable with the wavelengths simulated.
The best parameters of the optimization routine have been used to grow and process thin-film heterojunctions. The measurements results are reported in the table below.

Thin-Film Measurements			
Coverage[%]	V_{oc}[V]	J_{sc}[mAcm^{-2}]	Fill Factor
1.7	1.095	29.4	56.3

The results are very encouraging. Both the short-circuit current density and the open-circuit voltage are higher than the best ever achieved at the Applied Material Science department at Radboud University for this kind of cells. While J_{SC} is slightly higher, the open-circuit voltage is $\sim$ 20mV bigger than the second best result ever achieved for this kind of cells.
The very low Fill Factor is due to the fact that during the processing, some practical problems arose leading to a 100nm Gold layer as top metal contact. Generally, for this coverage percentage, in order to ensure a not too high series resistance, a 5um Gold layer is used for the top contact. For this reason, the overall performance of the cell was toppled by this unplanned feature.

The external quantum efficiencies were also measured and compared with the simulated ones. The results are plotted in Fig.5.4.

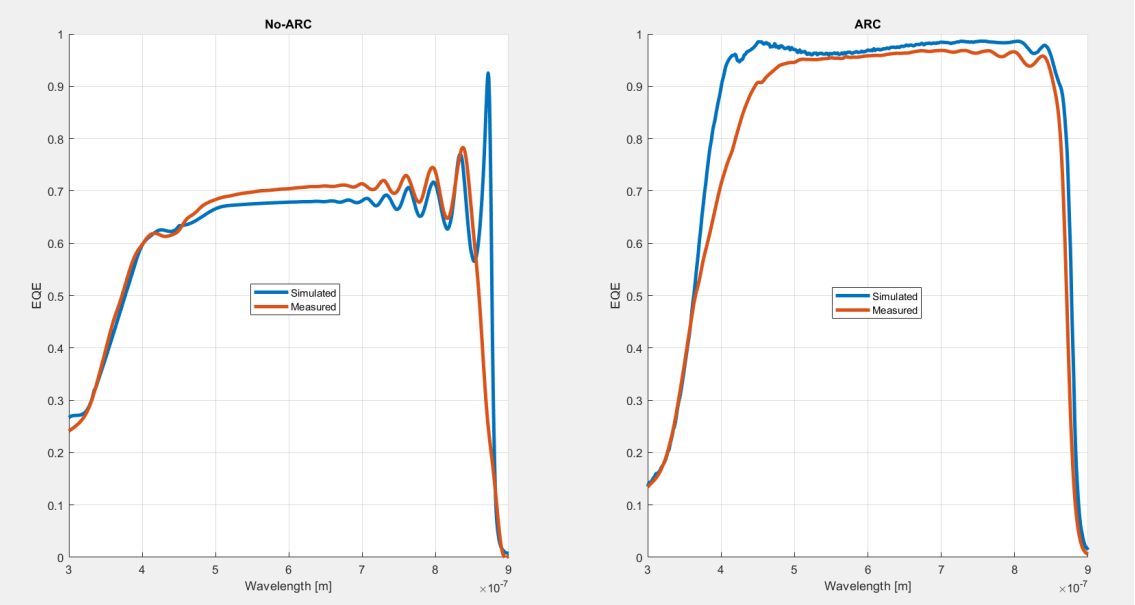

Figure 5.4: Measured and Simulated EQEs for the optimized thin-film cell structure. The red lines are the experimental ones and the blue lines are the theoretical ones. The GaAs complex refractive index data used have been taken from online databases

A slight underestimation of the EQE for the "central" wavelengths is present in the simulated thin film EQE without anti-reflection coating. This is in agreement with what has been found for the substrate cells since, in this case, the emitter thickness is close to $2[um]$. More noticeably, the oscillations of the two curves are not perfectly alligned. This is due to the definition of the GaAs complex refractive index: in fact, decreasing slightly the real part of the complex refractive index data for Gallium Arsenide with respect to the ones found on online databases, a much better fit for the EQE is obtained (see Fig.5.5).

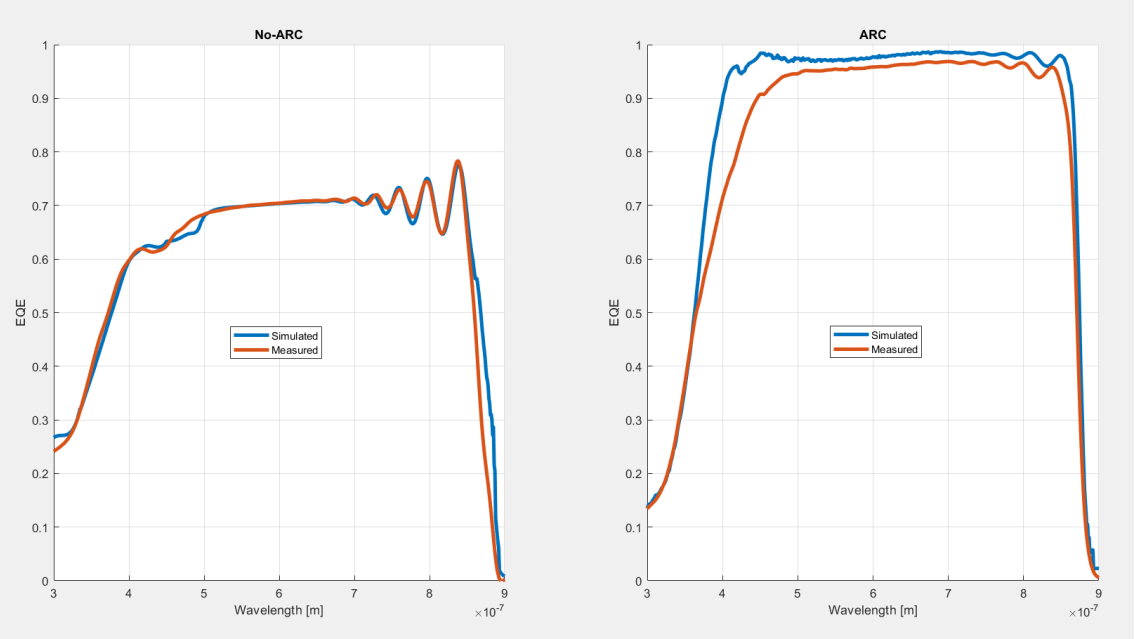

Figure 5.5: Measured and Simulated EQEs for the optimized thin-film cell structure. The red lines are the experimental ones and the blue lines are the theoretical ones. The GaAs complex refractive index data used have been slightly altered from the database ones

A similar problem affects the simulated EQE of the thin film cell with anti-reflection coating. In fact, even using the modified data for GaAs, the simulated EQE overestimate the experimental one for the cell with ARC. Considering that the same cell have been measured before and after the deposition of the anti-reflection coating, the differences must be due to the incorrect definition of MgF_2 and ZnS complex refractive indexes.

6 | Conclusions and Outlook

In this work, a new, innovative method to characterize the emitter-window interface of a solar cell has been developed.
A series of cells have been grown, processed and measured in order to investigate the relation between the emitter-window surface recombination speed and the emitter thickness and doping and, ultimately, the excess minority carriers at the interface.
The dependency of the S_f values on p'_{int}, other than on the interface quality, has been shown. The relation between the surface recombination speed and the doping levels appears to be well defined and led us to think that, increasing the excess minority carriers at the interface, the surface recombination speed of the said interface would decrease. This behaviour was not confirmed by the sets of cells with variable emitter thickness, which displayed an oscillatory relation between the n-doped quasi-neutral region thickness and S_f. However, due to the limited resources and time at disposal, the study was restricted to certain ranges of the emitter thicknesses, making it more difficult to establish the overall behaviour of $S_f = S_f(d_1)$.
The Hovel model has been adapted to heterojunctions with promising results. Its relative simplicity with respect to models which solve the drift-diffusion+continuity equations numerically inside the junction has been exploited to make a relatively fast optimization program. The only relevant parameter for which there wasn't an analytical or empirical model was the top surface recombination speed. Considering the data derived from the experiments, a first, approximated empirical model relative to the GaAs-AlInP interfaces (created at the Applied Material Science at Radboud University) has been developed and used in the optimization routine. The results of the optimization routine vary considerably adopting different optical parameters to describe the materials. The results allowed us to grow and process a thin-film GaAs-InGaP heterojunction solar cell with an excellent open-circuit voltage and a good short-circuit current.

This work suggests multiple potential avenues of study.
It would be very interesting to investigate further the relation between the emitter thickness and the emitter-window surface recombination speed and, ultimately, the one between the excess minority carriers and S_f. This can be achieved by growing and processing cells with higher emitter thicknesses (comparable and higher than the GaAs hole diffusion length).
Furthermore, a more in depth study of the causes of the oscillatory behaviour of the surface recombination speed vs the emitter thickness curves might be very interesting in order to better understand the effects of the optical dynamics on the electrical behaviour of the cells.
Finally, in order to best exploit the potential of the Hovel model (and of every other model simulating solar cells), reliable and simple techniques to derive experimentally the complex refractive indexes of the materials grown in a clean room must be integrated in every experimental department. Using simple and readily available equipment in a scientific department dealing with solar cells, reflectances and transmittances of a layer of whatever material can be measured; exploiting a simple scattering matrix method, such as the one developed for this work, the complex refractive indexes of the grown material can be fitted for each wavelength.

7 | Acknowledgements

I want to thank my wonderful family for the incredible support they always gave me during the years. They have been fundamental for my personal growth since I was a child and I will always be immensely grateful to them for all the love and help they provided.
I would also like to thank my supervisor Federica Cappelluti for giving me the opportunity to grow professionally and for the multiple insights she gave me.
Last but not least, I am very thankful to the team at the Applied Material Science department at Radboud University. They have been extremely helpful both practically and by creating a very friendly work environment. In this regard, a special thank goes to Gerard Bauhuis who guided me in my research.

Bibliography

[1] Sotoodeh, M., A. H. Khalid, and A. A. Rezazadeh. "Empirical low-field mobility model for III–V compounds applicable in device simulation codes." Journal of applied physics 87.6 (2000): 2890-2900.

[2] Lumb, Matthew P., et al. "Incorporating photon recycling into the analytical drift-diffusion model of high efficiency solar cells." Journal of Applied Physics 116.19 (2014): 194504.

[3] Van Roosbroeck, W., and W. Shockley. "Photon-radiative recombination of electrons and holes in germanium." Physical Review 94.6 (1954): 1558.

[4] Steiner, M. A., et al. "Optical enhancement of the open-circuit voltage in high quality GaAs solar cells." Journal of Applied Physics 113.12 (2013): 123109.

[5] Pellegrino, Carmine, Alessio Gagliardi, and Claus G. Zimmermann. "Difference in space [U+2010] charge recombination of proton and electron irradiated GaAs solar cells." Progress in Photovoltaics: Research and Applications 27.5 (2019): 379-390.

[6] Belghachi, A. "Modelling of perimeter recombination in GaAs solar cells." Microelectronics journal 36.2 (2005): 115-124.

[7] Lumb, Matthew P., et al. "Extending the 1-D hovel model for coherent and incoherent back reflections in homojunction solar cells." IEEE Journal of Quantum Electronics 49.5 (2013): 462-470.

[8] Sun, Yubo, Allison Perna, and Peter Bermel. "Comparing front-and rear-junction GaInP photovoltaic devices through detailed numerical and analytical modeling." IEEE Journal of Photovoltaics 9.2 (2019): 437-445.

[9] Thomeer, Robert AJ. Time-resolved photoluminescence experiments on different III-V semiconductor structures. Diss. Radboud University Nijmegen, 1995.

[10] Partain, L. D., et al. "A new sequentially etched quantum [U+2010] yield technique for measuring surface recombination velocity and diffusion lengths of solar cells." Journal of applied physics 61.11 (1987): 5150-5158.

[11] Partain, L. D., et al. "Diffusion length and interface recombination velocity measurement of a GaAs solar cell using two emitter fabrications and quantum yield." Solar cells 28.3 (1990): 223-232.

[12] http://www.ioffe.ru/SVA/

[13] Qi, Boyuan, and Jizheng Wang. "Fill factor in organic solar cells." Physical Chemistry Chemical Physics 15.23 (2013): 8972-8982.

[14] Shanawani, Mazen Masotti, Diego Costanzo, Alessandra. (2017). THz Rectennas: Rectification Prospects Challenges.

[15] https://www.nrel.gov/pv/cell-efficiency.html

[16] Gruginskie, N. Thin-Film III-V Solar Cells. Photon Recycling and Space Application Testing. Diss. [Sl: sn], 2020.

8 | Appendix A - Scattering Matrix Method

We define,

$$n_m^z = \sqrt[p]{n_m^2 - (n_0 sin(\theta))^2} \tag{8.1}$$

where the "p" stands for the fact that between the two square roots of the argument complex number the one with the negative imaginary part is chosen, and:

$$k_m^z = \frac{2\pi}{\lambda} n_m^z \tag{8.2}$$

The scattering matrix method relies on building the so-called "scattering matrices" here defined relative to Fig.8.1:

- Interfaces:

$$\begin{pmatrix} E_{m-1}^- \\ E_m'^+ \end{pmatrix} = S_{\text{int}}^m * \begin{pmatrix} E_{m-1}^+ \\ E_m'^- \end{pmatrix}, S_{\text{int}}^m = \begin{pmatrix} S_{11\text{int}}^m & S_{12\text{int}}^m \\ S_{21\text{int}}^m & S_{22\text{int}}^m \end{pmatrix} \tag{8.3}$$

  with:

  - * For TE:

$$S_{11\text{int}}^m = \frac{n_{m-1}^z - n_m^z}{n_{m-1}^z + n_m^z} \tag{8.4}$$

    * For TM:

$$S_{11\text{int}}^m = \frac{n_m^2 n_{m-1}^z - n_{m-1}^2 n_m^z}{n_m^2 n_{m-1}^z + n_{m-1}^2 n_m^z} \tag{8.5}$$

  - * For TE:

$$S_{12\text{int}}^m = \frac{2n_m^z}{n_{m-1}^z + n_m^z} \tag{8.6}$$

    * For TM:

$$S_{12\text{int}}^m = \frac{2n_m n_{m-1} n_m^z}{n_m^2 n_{m-1}^z + n_{m-1}^2 n_m^z} \tag{8.7}$$

  - * For TE:

$$S_{21\text{int}}^m = \frac{2n_{m-1}^z}{n_{m-1}^z + n_m^z} \tag{8.8}$$

    * For TM:

$$S_{21\text{int}}^m = \frac{2n_m n_{m-1} n_{m-1}^z}{n_m^2 n_{m-1}^z + n_{m-1}^2 n_m^z} \tag{8.9}$$

  - * For TE:

$$S_{22\text{int}}^m = -S_{11\text{int}}^m \tag{8.10}$$

    * For TM:

$$S_{22\text{int}}^m = -S_{11\text{int}}^m \tag{8.11}$$

- Layers:

$$\begin{pmatrix} E'^{-}_m \\ E^{+}_m \end{pmatrix} = S^m_{\text{lay}} * \begin{pmatrix} E'^{+}_m \\ E^{-}_m \end{pmatrix}, S^m_{\text{lay}} = \begin{pmatrix} S^m_{11\text{lay}} & S^m_{12\text{lay}} \\ S^m_{21\text{lay}} & S^m_{22\text{lay}} \end{pmatrix} \tag{8.12}$$

with:

  - $$S^m_{11\text{lay}} = 0 \tag{8.13}$$

  - $$S^m_{12\text{lay}} = e^{-jk^z_m t_m} \tag{8.14}$$

  - $$S^m_{21\text{lay}} = e^{-jk^z_m t_m} \tag{8.15}$$

  - $$S^m_{22\text{lay}} = 0 \tag{8.16}$$

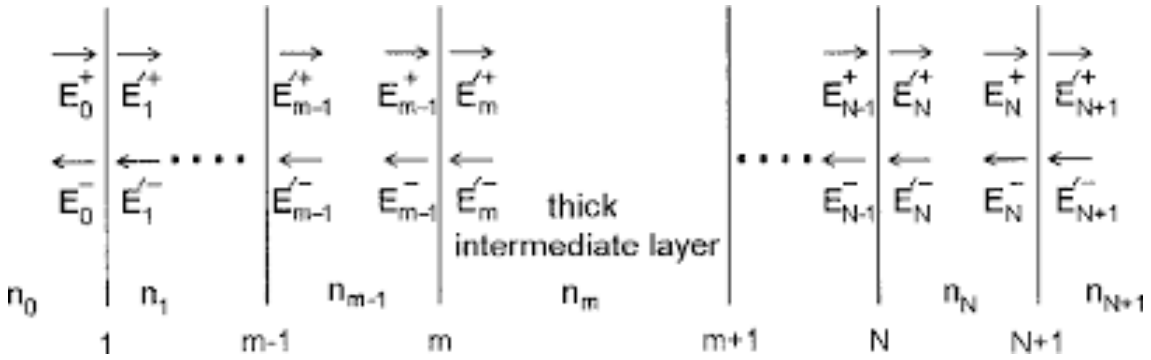

Figure 8.1: General layer stack

Overall, we have:

$$\begin{pmatrix} E^{-}_0 \\ E'^{+}_{N+1} \end{pmatrix} = S_{\text{tot}} * \begin{pmatrix} E^{+}_0 \\ E'^{-}_{N+1} \end{pmatrix}, S_{\text{tot}} = \begin{pmatrix} S_{11\text{tot}} & S_{12\text{tot}} \\ S_{21\text{tot}} & S_{22\text{tot}} \end{pmatrix} \tag{8.17}$$

with:

$$S_{\text{tot}} = S^0_{\text{int}} \otimes S^1_{\text{lay}} \otimes S^1_{\text{int}} \otimes S^2_{\text{lay}} \otimes ... \otimes S^{N-1}_{\text{int}} \otimes S^N_{\text{lay}} \otimes S^N_{\text{int}} \tag{8.18}$$

Where $S^{AB} = S^A \otimes S^B$ consists in:

- $$S^{AB}_{11} = S^A_{11} + \frac{S^A_{12} * S^B_{11} * S^A_{21}}{1 - S^B_{11} * S^A_{22}} \tag{8.19}$$

- $$S^{AB}_{12} = \frac{S^A_{12} * S^B_{12}}{1 - S^B_{11} * S^A_{22}} \tag{8.20}$$

- $$S^{AB}_{21} = \frac{S^B_{21} * S^A_{21}}{1 - S^B_{11} * S^A_{22}} \tag{8.21}$$

- $$S^{AB}_{22} = S^B_{22} + \frac{S^B_{21} * S^A_{22} * S^B_{12}}{1 - S^B_{11} * S^A_{22}} \tag{8.22}$$

The total scattering matrix elements (S_{ii}^{tot}) can be easily derived.

The first and last media are considered to be lossless ($\alpha'_0 = \alpha'_{N+1} = 0$) and the last medium is considered to have infinite thickness so that $E'^{-}_{N+1} = 0$. From here, it is straightforward to define reflectances and transmittances of the whole layer stack:

$$r^{\text{TE/TM}}(\lambda,\theta) = \frac{\mathcal{E}^{\text{TE/TM}}_{\text{reflected}}}{\mathcal{E}^{\text{TE/TM}}_{\text{incident}}} = {S_{11}^{\text{TE/TM}}}_{\text{tot}} \tag{8.23}$$

$$t^{\text{TE/TM}}(\lambda,\theta) = \frac{\mathcal{E}^{\text{TE/TM}}_{\text{transmitted}}}{\mathcal{E}^{\text{TE/TM}}_{\text{incident}}} = {S_{21}^{\text{TE/TM}}}_{\text{tot}} \tag{8.24}$$

$$R^{\text{TE/TM}}(\lambda,\theta) = \frac{P^{\text{TE/TM}}_{\text{opt,reflected}}}{P^{\text{TE/TM}}_{\text{opt,incident}}} = |r^{\text{TE/TM}}|^2 \tag{8.25}$$

$$T^{\text{TE/TM}}(\lambda,\theta) = \frac{P^{\text{TE/TM}}_{\text{opt,transmitted}}}{P^{\text{TE/TM}}_{\text{opt,incident}}} = |t^{\text{TE/TM}}|^2 * \left(\frac{n^z_{N+1}}{n^z_0}\right) \tag{8.26}$$

In our situation, it is assumed that the impinging wave is on average half "TE" and half "TM" so that the overall reflectances and transmittances can be defined as:

$$R = \frac{1}{2}R^{\text{TE}} + \frac{1}{2}R^{\text{TM}} \tag{8.27}$$

$$T = \frac{1}{2}T^{\text{TE}} + \frac{1}{2}T^{\text{TM}} \tag{8.28}$$

9 | Appendix B - Electrical Model

Starting from the drift-diffusion + continuity equations in steady state $\left(\frac{\partial}{\partial t} = 0\right)$, assuming negligible electric field (hence negligible drift current) in the quasi-neutral regions, it is straightforward to derive the following second order differential equations:

- n-QNR:

$$\frac{d^2p'}{dx^2} - \frac{p'}{L_p^2} + \frac{1}{D_p}\int_0^{+\infty} \alpha\Phi(\lambda, x)d\lambda = 0 \tag{9.1}$$

- p-QNR:

$$\frac{d^2n'}{dx^2} - \frac{n'}{L_n^2} + \frac{1}{D_n}\int_0^{+\infty} \alpha\Phi(\lambda, x)d\lambda = 0 \tag{9.2}$$

The last two terms of both equations come from the approximated recombination and generation rates respectively, of the excess minority carriers:

$$U_{\mathrm{p,Tot}} = \frac{p'}{\tau_p} \tag{9.3}$$

$$U_{\mathrm{n,Tot}} = \frac{n'}{\tau_n} \tag{9.4}$$

and,

$$G_{\mathrm{p,Tot}} = \int_0^{+\infty} \alpha\Phi(\lambda, x)d\lambda \tag{9.5}$$

$$G_{\mathrm{n,Tot}} = \int_0^{+\infty} \alpha\Phi(\lambda, x)d\lambda \tag{9.6}$$

From the theory of n-p junctions, the boundary conditions are:

- Boundary Conditions n-QNR:

$$p'(x = d_1) = \frac{n_i^2}{N_D}\left(e^{\frac{V}{V_T}} - 1\right), \frac{dp'}{dx}|_{x=0} = \frac{S_p}{D_p}p'(x = 0) \tag{9.7}$$

- Boundary Conditions p-QNR:

$$n'(x = d_1 + W) = \frac{n_i^2}{N_A}\left(e^{\frac{V}{V_T}} - 1\right), \frac{dn'}{dx}|_{x=P} = -\frac{S_n}{D_n}n'(x = P) \tag{9.8}$$

Finally, assuming a perfect collection efficiency of the electron-hole (e-h) pairs generated in the space charge region and neglecting any kind of recombination inside it, the e-h pairs generated are given by the integral of the absorption coefficient times the photon-flux over all the wavelengths:

$$J_W = q\int_0^{+\infty} \alpha\Phi(\lambda, x)d\lambda \tag{9.9}$$

Eq.9.1 and Eq.9.2 are non-homogeneous differential equation which can be solved using the "method of variation of constants". Ones the expressions for $p'(x)$ and $n'(x)$ are obtained, the diffusion current densities in the quasi-neutral regions are computed:

$$J_p^{\text{Tot}} = -qD_p \frac{dp'}{dx}|_{x=d_1} \tag{9.10}$$

$$J_n^{\text{Tot}} = qD_n \frac{dn'}{dx}|_{x=d_1+W} \tag{9.11}$$

Overall, it is obtained:

- n-doped QNR (Emitter):

$$J_p^{\text{Tot}} = J_p^{\text{Photo}} + J_p^{\text{Dark}} \tag{9.12}$$

where:

$$J_p^{\text{Dark}} = -\left(\frac{qD_p n_i^2}{L_p N_D} \frac{\sinh\left(\frac{d_1}{L_p}\right) + \frac{S_p L_p}{D_p}\cosh\left(\frac{d_1}{L_p}\right)}{\cosh\left(\frac{d_1}{L_p}\right) + \frac{S_p L_p}{D_p}\sinh\left(\frac{d_1}{L_p}\right)}\right)\left(e^{\frac{V}{V_T}} - 1\right) \tag{9.13}$$

$$J_p^{\text{Photo}} = \int_0^{+\infty} F_p \left[\frac{\frac{\partial z_p}{\partial x}|_{x=0} - \frac{S_p}{D_p} z_p(\lambda, 0)}{\cosh\left(\frac{d_1}{L_p}\right) + \frac{S_p L_p}{D_p}\sinh\left(\frac{d_1}{L_p}\right)} + \frac{r_p}{L_p} z_p(\lambda, d_1) - \frac{\partial z_p}{\partial x}|_{x=d_1}\right] d\lambda \tag{9.14}$$

with:

$$F_p = \frac{q\Phi_0 T_f L_p^2 \alpha_A}{1 + R_b R_f e^{-2\alpha_A L} - 2e^{-\alpha_A L} Re\left(r_b r_f e^{-j\beta_A L}\right)} \tag{9.15}$$

$$z_p = \frac{e^{-\alpha_A x}}{1 - (\alpha L_p)^2} + \frac{R_b e^{-2\alpha_A L} e^{\alpha_A x}}{1 - (\alpha_A L_p)^2} + \frac{2e^{-\alpha_A L}}{1 + (\beta_A L_p)^2} Re\left(r_b e^{-j\beta_A L} e^{j\beta_A x}\right) \tag{9.16}$$

$$r_p = \frac{\sinh\left(\frac{d_1}{L_p}\right) + \frac{S_p L_p}{D_p}\cosh\left(\frac{d_1}{L_p}\right)}{\cosh\left(\frac{d_1}{L_p}\right) + \frac{S_p L_p}{D_p}\sinh\left(\frac{d_1}{L_p}\right)} \tag{9.17}$$

- p-doped QNR (Base):

$$J_n^{\text{Tot}} = J_n^{\text{Photo}} + J_n^{\text{Dark}} \tag{9.18}$$

where:

$$J_n^{\text{Dark}} = -\left(\frac{qD_n n_i^2}{L_n N_D} \frac{\sinh\left(\frac{d_2}{L_n}\right) + \frac{S_n L_n}{D_n}\cosh\left(\frac{d_2}{L_n}\right)}{\cosh\left(\frac{d_2}{L_n}\right) + \frac{S_n L_n}{D_n}\sinh\left(\frac{d_2}{L_n}\right)}\right)\left(e^{\frac{V}{V_T}} - 1\right) \tag{9.19}$$

$$J_n^{\text{Photo}} = \int_0^{+\infty} F_n \left[-\frac{\frac{\partial z_n}{\partial x}|_{x=L} + \frac{S_n}{D_n} z_n(\lambda, L)}{\cosh\left(\frac{d_2}{L_n}\right) + \frac{S_n L_n}{D_n}\sinh\left(\frac{d_2}{L_n}\right)} + \frac{r_n}{L_n} z_n(\lambda, x_p) + \frac{\partial z_n}{\partial x}|_{x=x_p}\right] d\lambda \tag{9.20}$$

with:

$$F_n = \frac{q\Phi_0 T_f L_n^2 \alpha_A}{1 + R_b R_f e^{-2\alpha_A L} - 2e^{-\alpha_A L} Re\left(r_b r_f e^{-j\beta_A L}\right)} \tag{9.21}$$

$$z_n = \frac{e^{-\alpha_A (x+d_E)}}{1 - (\alpha_A L_n)^2} + \frac{R_b e^{-2\alpha_A L} e^{\alpha_A (x+d_E)}}{1 - (\alpha_A L_n)^2} + \frac{2e^{-\alpha_A L}}{1 + (\beta_A L_n)^2} Re\left(r_b e^{-j\beta_A L} e^{j\beta_A (x+d_E)}\right) \tag{9.22}$$

$$r_n = \frac{\sinh\left(\frac{d_2}{L_n}\right) + \frac{S_n L_n}{D_n}\cosh\left(\frac{d_2}{L_n}\right)}{\cosh\left(\frac{d_2}{L_n}\right) + \frac{S_n L_n}{D_n}\sinh\left(\frac{d_2}{L_n}\right)} \tag{9.23}$$

- SCR (Depleted Region):

$$J_W^{\text{Tot}} = J_W^{\text{Photo}} \tag{9.24}$$

where:

$$J_W^{\text{Photo}} = \int_0^{+\infty} F_W \left(z_{W,1} + z_{W,2} + z_{W,3}\right) d\lambda \tag{9.25}$$

with:

$$F_W = \frac{q\Phi_0 T_f}{1 + R_b R_f e^{-2\alpha_A L} - 2e^{-\alpha_A L} Re\left(r_b r_f e^{-j\beta_A L}\right)} \tag{9.26}$$

$$z_{W,1} = e^{-\alpha_A d_1}\left(1 - e^{-\alpha_A W}\right) \tag{9.27}$$

$$z_{W,2} = R_b e^{-\alpha_A (2L - d_1)}\left(e^{\alpha_A W} - 1\right) \tag{9.28}$$

$$z_{W,3} = 2\frac{\alpha_A}{\beta_A} e^{-\alpha_A L} Im\left(r_b e^{-j\beta_A (L - d_1)}\left(e^{j\beta_A W} - 1\right)\right) \tag{9.29}$$

10 | Appendix C - Input Parameters

Simulations Inputs	
Parameter	Value
GaAs band gap	1.424eV
GaAs electron affinity	4.07eV
GaAs relative dielectric constant	12.9
GaAs effective conduction band carrier concentration	$4.7 \times 10^{17}\text{cm}^{-3}$
GaAs effective valence band carrier concentration	$9 \times 10^{18}\text{cm}^{-3}$
GaAs intrinsic carrier concentration	$2.1 \times 10^{6}\text{cm}^{-3}$
GaAs mobilities	From [1]
GaAs radiative lifetimes	Analytically derived (2.2.2)
GaAs SRH lifetimes	From [2]
InGaP band gap	1.849eV
InGaP electron affinity	4.1eV
InGaP relative dielectric Constant	11.8
InGaP effective conduction band carrier concentration	$6.5 \times 10^{17}\text{cm}^{-3}$
InGaP effective valence band carrier concentration	$1.45 \times 10^{19}\text{cm}^{-3}$
InGaP intrinsic carrier concentration	$2 \times 10^{3}\text{cm}^{-3}$
InGaP electron mobility	$0.1\text{m}^2\text{s}^{-1}\text{V}^{-1}$
InGaP hole mobility	$0.034\text{m}^2\text{s}^{-1}\text{V}^{-1}$
InGaP radiative lifetimes	Analytically derived (2.2.2)
InGaP SRH lifetimes	3×10^{-9}
GaAs-InGaP surface recombination speed	1.5cms^{-1}

The used incident photon-flux as a function of the wavelengths is plotted in Fig.10.1.

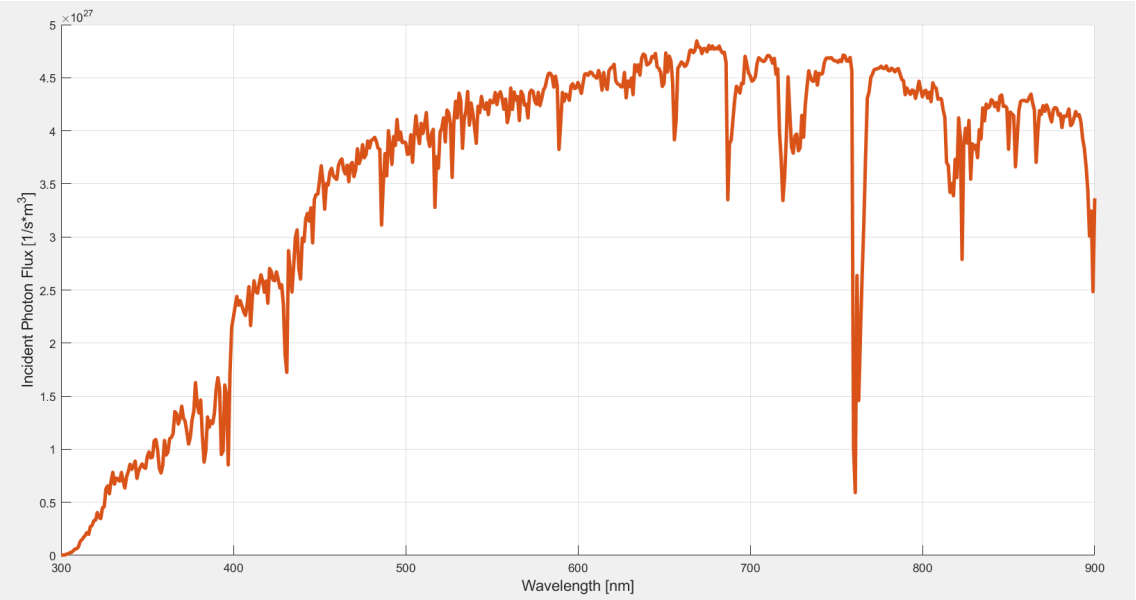

Figure 10.1: Used incident photon-flux as a function of wavelengths

The used complex refractive indexes as a function of wavelengths are plotted in Fig.10.2 and Fig.10.3.

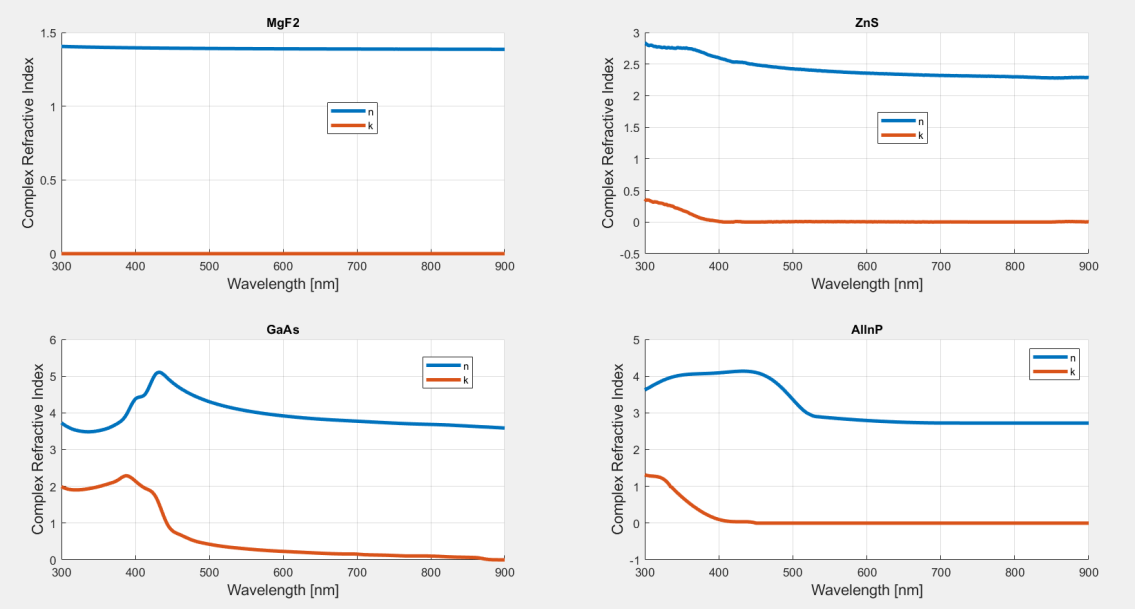

Figure 10.2: Used MgF_2, ZnS, GaAs and AlInP complex refractive indexes as a function of wavelengths

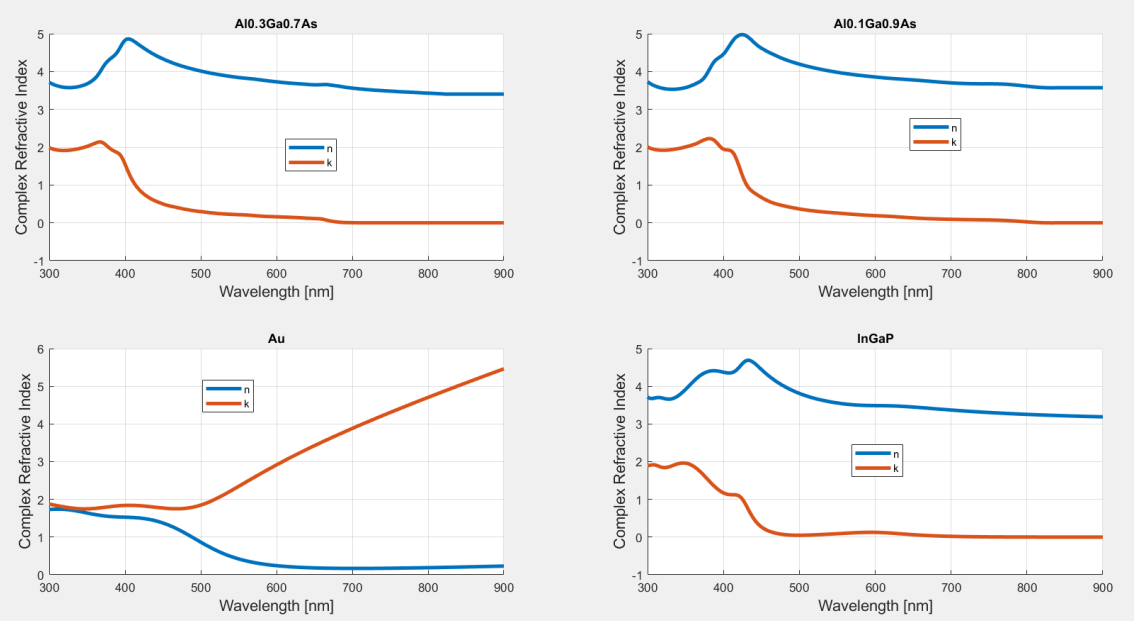

Figure 10.3: Used $Al_{0.3}Ga_{0.7}As$, $Al_{0.1}Ga_{0.9}As$, Au and InGaP complex refractive indexes as a function of wavelengths